Parametric investigation on the performance-emissions trade-off and knocking occurrence of dual fuel engines using CFD

La Xiang[a,b], Gerasimos Theotokatos[b], Yu Ding[a,*]

[a] *College of Power and Energy Engineering, Harbin Engineering University, Harbin, China*

[b] *Maritime Safety Research Centre, Department of Naval Architecture, Ocean and Marine Engineering, University of Strathclyde, Glasgow, Scotland, UK*

[*] *Corresponding author: e-mail: dingyu@hrbeu.edu.cn; address: No. 145, Nantong Street, 150001, Harbin, China*

Abstract

Dual fuel (DF) engines have been an attractive alternative of traditional diesel engines for reducing both the environmental impact and operating cost. The major challenge of DF engine design is to deal with the performance-emissions trade-off via operating settings optimisation. This study aims at parametrically investigating the engine settings optimisation for a simultaneous reduction of NOx emissions and brake specific fuel consumption (BSFC) of marine DF engines while avoiding knocking accurrence by using a computational fluid dynamics (CFD) model. The model is developed in the CONVERGE software and validated by employing the measured in-cylinder pressure and emissions. Subsequently, the model is used to parametrically investigate the engine operating settings (pilot injection timing, equivalence ratio and natural gas mass) that allow simultaneous reduction of NOx and BSFC emissions at three engine operating conditions (1800 r/min, 1629 r/min and 1457 r/min). Result shows that the optimal solution at 1800 r/min and 1629 r/min operation conditions can be achieved by controlling the pilot injection timing, equivalence ratio variation and NG mass variation within –5 to –7.5 °CA, –5% to +5% and 0% to +20%, respectively. For the 1457 r/min operation condition, the

appropriate ranges of pilot injection timing and the equivalence ratio variation are the same with those

at 1800 r/min and 1629 r/min, whilst the NG mass variation range should be between –10% and +10%.

The derived results in this study are expected to support the combustion analysis and enhancement of

marine DF engines during the design phase, whilst the derived optimal solution is expected to provide

guidelines of DF engine management for reducing operating cost and environmental footprint.

Keywords: dual fuel engines; performance-emissions trade-off, knocking, parametric investigation, CFD simulation model

Highlights
(1) Dual fuel engine CFD modelling in CONVERGE using CHEMKIN library
(2) Parametric optimization to simultaneously reduce NOx emissions and BSFC
(3) Study of engine settings effects on performance, emissions and knocking occurrence
(4) Potential for reducing NOx emissions by 9.58% and BSFC by 3.25%

1. Introduction

To comply with the increasingly stringent marine emissions regulations, various solutions like combustion process optimisation [1-5], using after-treatment auxiliaries [6-8] and alternative fuels [9, 10], have been proposed for reducing the marine engine emissions, including Nitrogen Oxides (NOx), Sulphur Oxides (SOx) and Greenhouse Gas (CHG) emissions. Combustion process optimisation and using after-treatment auxiliaries are effective in reducing emissions but also increase the design cost and engine room arrangement, which make using alternative fuels an attractive option. Liquified Natural Gas (LNG), which is recognised as a zero-sulphur and low-carbon fuel, have an apparent positive effect on reducing NOx, SOx and GHG emissions [11, 12]. Thus, LNG has been gradually applied to marine internal combustion engines (ICE) replacing diesel and petrol for emissions reduction and efficiency improvement.

For marine applications, LNG is mainly used in the form of diesel-natural gas dual fuel (DF) engines, which employ a small amount of diesel fuel for initiating the natural gas (NG) ignition, as the NG has a lower cetane number and can barely be ignited by compression [13-16]. Diesel-NG DF engines show remarkable advantages of reducing NOx, SOx, particulate matter (PM) and carbon dioxide (CO_2) emissions, but usually are accompanied with increased brake specific fuel consumption (BSFC), unburnt hydrocarbon (UHC) and carbon monoxide (CO) emissions [17]. The reduction of Sox and CO_2 emissions can be easily explained by NG's zero-sulphur and low-carbon characteristics, whilst the NOx emissions reduction is mainly caused by the lower in-cylinder temperature due to the higher specific heat capacity of lean air-NG mixture [18]. On the other hand, the lower in-cylinder temperature results in lower brake thermal efficiency (BTE) and consequently higher BSFC. The NOx-BSFC trade-off of DF engines are apparent at low operating loads, whilst simultaneous reduction of NOx emissions and BSFC seems

possible at high operating loads [19].

Another challenge faced by the premixed combustion DF engines is the knocking phenomena, which is associated with the auto-ignition of the unburnt fuel-air mixture ahead of the flame front [20]. It is a common instability in the premixed combustion engines [21], which might cause severe damages to the combustion chamber structure [22]. For avoiding knocking occurrence, the NG-fuelled engines must operate at a relatively narrower air-fuel ratio range compared to diesel engines with similar dimensions. It is important to achieve the desired combustion behaviour whilst limiting the knocking occurrence. Since the knocking probability increases with higher in-cylinder temperature and pressure, the engine compression ratio must be kept below a maximum threshold for ensuring the engine knock-free operation. This, however, limits the engine efficiency.

As concluded from the above discussion, DF engines face several challenges in terms of their performance-emissions trade-off and knocking phenomena. Therefore, it is meaningful to study the combustion characteristics of DF engines and subsequently, use the obtained knowledge to optimise the engine design/operating settings for achieving better performance and less emissions.

Engine modelling and simulation contribute towards obtaining a better understanding of the engine components characteristics during the engine design phase; therefore, they can be employed for performing the engine settings optimisation. In general, simulation models for internal combustion engines can be classified as follows (from simpler to more complicated): mean value models, zero-dimensional (0D) or one-dimensional (1D) models, and three-dimensional (3D) Computational Fluid Dynamics (CFD) models [23]. The 3-D CFD models are capable of providing the most detailed analysis of the engine in-cylinder combustion processes when knocking occurs, adequately predicting the pre-flame reaction [24], the heat release rate [25] and emissions formation [26]; therefore, they are

4

appropriate for obtaining better insights of the involved physical-chemical processes in DF engines.

For characterising the combustion and emissions of NG-diesel DF engines, a number of studies have been carried out by using CFD simulation models. Maghbouli et al [27] proposed a CFD framework coupling with chemical kinetics, which was then employed for investigating the combustion and emission characteristics of a NG-diesel DF engine operating under different pilot fuel quantities. Chintala and Subramanian [28] conducted a CFD study for optimising the gas injector orientation (location and angle) for improving the brake thermal efficiency (BTE) of a DF engine operating on diesel-NG and diesel-H_2 mode. Mattarelli et al. [29] obtained the optimal settings of the premixed NG concentration and pilot diesel injection timing by using CFD, which rendered a converted DF engine achieving the same brake power with the baseline diesel engine, associated with significant reductions of soot, CO and CO_2 emissions. Maurya and Mishra [30] numerically investigated the effects of operating settings including engine speed, EGR mass percentage and NG premixing ratio on the combustion and emissions characteristics of a NG-diesel DF engine by using CFD approach. Li et al. [31] presented a numerical study on the combustion, spatial distribution and emissions of methane in a NG-diesel DF engine using a CFD simulation model coupled with a reduced primary reference fuel (PRF) mechanism. Shu et al [32] studied the effects of injection timing on the thermodynamics, combustion and emission (NOx and HC) characteristics of a NG-diesel DF engine at low speed and low load by using both CFD simulation and bench test. Most of the above-mentioned studies focused on individual settings effect on combustion and emissions of NG-diesel DF engines, few of them explored the combined effects and the optimal settings, which led to simultaneous reduction of NOx emission and BSFC. In addition, the knocking phenomenon has not been considered whilst investigating the performance and emissions of dual fuel engines.

For evaluating the effects of engine operating settings on knocking occurrence, experimental methods

are not extensively used in the early engine design phase due to their need for considerable resources and cost [33-36]. In this respect, a more cost-effective method to predict the knocking onset is by using simulation methods [37], which can be generally classified into three categories: (1) detailed chemical kinetic mechanisms for the pre-flame (or low-temperature) reactions [38, 39]; (2) simplified chemical kinetic mechanisms for the pre-flame reactions [40-42], and; (3) empirical formulas based on Arrhenius expression [43]. Detailed chemical kinetic mechanisms [38, 39] usually consider hundreds of species and thousands of elemental reactions, rendering the CFD model capable ofproviding detailed prediction of the local thermodynamic parameters including temperature, pressure and species concentration as well as the knocking onset. Nevertheless, this comes at the expense of huge computational cost, thus rendering this method not applicable in multi-variables and multi-objective optimisation studies based on engine cycle simulations [37]. Simplified chemical kinetic mechanisms were proposed to reduce the reactions number, which reduced the computational cost whilst maintaining acceptable prediction accuracy. Depending on the specific fuel type and application, the reactions number of these simplified mechanisms vary from several [40] to hundreds [41, 42]. To overcome the computation limitations, an one-step reaction formula was proposed by Livengood and Wu [43] by integrating the reciprocals of the unburnt zone autoignition delay that was estimated by using an Arrhenius expression. However, the prediction accuracy of Arrhenius-based formulas is low because the two-zone simplification of the in-cylinder space is not capable of characterising the combustion details. Thus, simplified chemical kinetic mechanisms coupled with CFD models could be a cost-effective way for predicting the knocking occurrence considering the computational cost and prediction accuracy.

This study aims at parametrically investigating the engine settings optimisation for simultaneously reducing both NOx emissions and brake specific fuel consumption (BSFC) of marine DF engines whilst

avoiding knocking occurrence. To this end, a 3D CFD model is developed and coupled with a simplified chemical kinetic mechanism of Diesel/NG combustion in the CONVERGE software. This model is validated by using the measured in-cylinder pressure and emissions parameters. Subsequently, the validated model is used to investigate the effect of single operating setting on the in-cylinder combustion characteristics, knocking occurrence, performance and emissions of the investigated DF engine. Lastly, a parametric study is performed to identify the optimal operating settings for NOx emission and BSFC reduction at three operating conditions.

The novelty of this study is summarised as follows: (a) comprehensive investigation on both in-cylinder combustion (temperature distribution, NOx emissions formation, knocking occurrence) and engine performance parameters (pressure, heat release rate, IMEP and BSFC) of marine DF engines; (b) parametric investigation indicating the potential engine operating settings that could provide a simultaneous reduction of BSFC and NOx emissions whilst avoiding knocking occurrence.

2.   Modelling Methodology

This section describes the 3D CFD simulation model employed in this study in order to investigate the combustion characteristics and knocking performance of DF engines. The developed model was implemented in the CONVERGE computational environment, which is featured with autonomous meshing, state-of-the-art physical models, advanced chemistry solver and the prominent ability of accommodating complex moving geometries [44]. A number of sub-models are used for characterising the diesel injection, spray and injection, combustion, turbulence, etc.

2.1 Calculation Principles

In the proposed 3D CFD simulation model, the statement of the in-cylinder mixture is governed by the conservation equations of mass transport, momentum transport and energy transport, as well as the ideal gas state equation. Table 1 lists the employed mathematical models and chemical mechanisms along with

the pertinent studies that provide the detailed description. The Blob injection model [45], the KH-RT

model [46] and the Frossling model [47] were selected to simulate the injection, breakup and evaporation

process of the pilot diesel, respectively. The SAGE model [48] was used for simulating the combustion

process, whilst the detailed chemical kinetic was characterised via the optimised GRI-Mech 3.0 and

Valeri coupling mechanism [49]. The NOx emissions were calculated by using the Extended Zeldovich

mechanism [20]. In addition, the RNG k-ε model [50] and the O 'Rourke-Amsden model [51] were

employed to characterise the in-cylinder turbulence and heat transfer. The governing equations, pilot

injection sub-model, spray breakup sub-model, evaporation sub-model, combustion sub-model and

turbulence sub-model are introduced in the following sections.

Table 1 Employed mathematical models and chemical mechanisms in the 3D CFD simulation model

Models/mechanisms	Sub-model	Brief introduction
Pilot injection	Blob model	In Blob injection model, the injected drop sizes are considered to be equal to the nozzle diameter or effective diameter.
Spray breakup	KH-RT model	The KH-RT model is the concurrent application of the Kelvin-Helmholtz [52] and the Rayleigh-Taylor [53] breakup models.
Evaporation	Frossling model	The mass transfer coefficient, liquid vapor mass diffusivity and Sherwood number are employed for evaluating the undisturbed droplet radius.
Combustion	SAGE model	SAGE calculates the reaction rates for each elementary reaction while the CFD solver solves the transport equations.
Reaction kinetics	Optimised GRI-Mech 3.0 and Valeri coupling mechanism	The optimised chemical kinetic mechanism includes 76 chemical species and 464 reactions, covering n-heptane and NG reactions.
Turbulence	RNG k-ε model	The Renormalisation Group (RNG) k-ε turbulence model shows better performance in characterising anisotropic and non-equilibrium effect than the standard k-ε turbulence model.
NOx formation	Extended Zeldovich mechanism	A third reaction accounting for the OH radicals influence is supplemented to the two reactions proposed by Zeldovich, which evaluate the NO formation from atmospheric nitrogen and oxygen.
Heat transfer	O 'Rourke-Amsden model	The molecular conductivity, Prandtl number, fluid temperature, wall temperature and shear speed are used for evaluating the heat transfer.

2.1.1 Governing equations

In CONVERGE, the dynamics of fluid flow are governed by equations that describe the conservation of

mass, momentum and energy. Additional equations describe the turbulence and the transport of passive scalars and species. The compressible equations for mass transport, momentum transport and energy transport are given by the following equations:

$$\frac{\partial \rho}{\partial t} + \frac{\partial \rho u_i}{\partial x_i} = S \tag{1}$$

$$\frac{\partial \rho u_i}{\partial t} + \frac{\partial \rho u_i u_j}{\partial x_j} = -\frac{\partial P}{\partial x_i} + \frac{\partial \sigma_{ij}}{\partial x_j} + S_i \tag{2}$$

$$\frac{\partial \rho e}{\partial t} + \frac{\partial u_j \rho e}{\partial x_j} = -P\frac{\partial u_j}{\partial x_i} + \sigma_{ij}\frac{\partial u_i}{\partial x_j} + \frac{\partial}{\partial x_j}\left(K\frac{\partial T}{\partial x_j}\right) + \frac{\partial}{\partial x_j}\left(\rho D \sum_m h_m \frac{\partial \gamma_m}{\partial x_j}\right) + S \tag{3}$$

Where, ρ is density; u is velocity, S is the source term; P is pressure; σ_{ij} is the stress tensor; e is the specific internal energy; K is the conductivity; D is the mass diffusion coefficient; h is the enthalpy; Y_m is the mass fraction of species m.

The Redlich-Kwong equation [54] is employed for characterising the gas state:

$$p = \frac{RT}{V-b} - \frac{a}{V^2 + ubV + wb^2} \tag{4}$$

Where, p is the pressure; R is the gas constant; T is the temperature; V is the volume; b, a, u, w are Redlich-Kwong coefficients that are reported in [44].

2.1.2 Injection, spray and evaporation models

To simulate the injection process, the core angle, nozzle position, orientation and hole size were inputted to model the injector geometry. N-heptane was used to represent the flow properties of diesel fuel. According to the Blob injection model [45], the injected drop sizes are considered to be equal to the nozzle diameter or effective diameter. The pilot injection mass, injection timing, injection duration and injection pressure are used as input to calculate the injection mass flow. Since the pilot diesel is supplied by a common-rail system in the investigated engine, the injection pressure is considered to be constant during the injection duration.

The KH-RT breakup length model [46] is the concurrent application of the Kelvin-Helmholtz [52] and

the Rayleigh-Taylor [53] breakup models. This model assumes that only KH instabilities are responsible

for drop breakup inside of the characteristic breakup distance L_b, while both KH and RT mechanisms are

activated beyond the breakup length. When the KH-RT model is activated, the break length L_b can be

specified according to Eq (5).

$$L_b = C_{bl}\sqrt{\frac{\rho_l}{\rho_g}}r_p \tag{5}$$

Where, C_{bl} is the break length constant [55], which can be tuned to increase or decrease spray breakup

by changing the parameter *distant* in spray input document; ρ_l and ρ_g are the density of liquid and gas; r_p

is the droplet radius before breakup.

The Frossling [47] vaporisation correlation is expressed by the following equation:

$$\frac{dr_0}{dt} = -\frac{\alpha_{spray}\rho_g D}{2\rho_l r_0}B_d Sh_d \tag{6}$$

Where, r_0 is the undisturbed droplet radius; α_{spray} is the user-specified scaling factor for the mass transfer

coefficient; D is the mass diffusivity of liquid vapor in air; B_d is determined by the vapor mass fraction;

Sh_d is the Sherwood number.

2.1.3 Combustion model

The SAGE solver [48], which models detailed chemical kinetics via a set of CHEMKIN-formatted input

files, was selected to simulate the combustion of the dual fuel engine. SAGE calculates the reaction rates

for each elementary reaction while the CFD solver solves the transport equations. The mechanism of the

multi-step chemical reaction [56] is described by Eq (7).

$$\sum_{m=1}^{M} v'_{m,r}\chi_m \Leftrightarrow \sum_{m=1}^{M} v''_{m,r}\chi_m \qquad \text{for } r = 1, 2, ...R \tag{7}$$
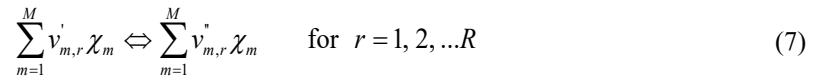
Where, $v'_{m,r}$ and $v''_{m,r}$ are the stoichiometric coefficients for the reactants and products, respectively,

for species m and reaction r; R is the total number of reactions; χ_m *is* the chemical symbol for species m.

The net production rate of species m is given the following equation.

$$\dot{\omega}_m = \sum_{r=1}^{R} v_{m,r} q_r \quad \text{for} \quad m = 1, 2, \dots M \tag{8}$$

Where, M is the total number of species; q_r is the rate-of-progress parameter.

With the above information, the following governing equation for energy conservation can be solved for a given computational cell:

$$\frac{dT}{dt} = \frac{V \dfrac{dP}{dt} - \sum_m (\bar{h}_m \dot{\omega}_m)}{\sum_m (\bar{c}_{p,m} \cdot \int \dot{\omega}_m dt)} \tag{9}$$

Where, $\bar{h}_m$ is the molar specific enthalpy; $\bar{c}_{p,m}$ is the molar specific heat at constant pressure.

2.1.4 Turbulence model

As turbulence significantly affects the mixing rate of momentum, energy and species, a turbulence model must be included to attain accurate CFD simulation results. The Renormalisation Group (RNG) *k-ε* turbulence model [50], which shows better performance in characterising anisotropic and non-equilibrium effect than the standard *k-ε* turbulence model, is employed to model the in-cylinder turbulence. The transport equation of turbulent kinetic energy *k* and the dissipation of turbulent kinetic energy *ε* are given by Eq (10) and Eq (11).

$$\frac{\partial \rho k}{\partial t} + \frac{\partial \rho u_i k}{\partial x_i} = \tau_{ij} \frac{\partial u_i}{\partial x_i} + \frac{\partial}{\partial x_j} \frac{\mu + \mu_t}{P_{r_k}} \frac{\partial k}{\partial x_j} - \rho\varepsilon + \frac{C_S}{1.5} S_S \tag{10}$$

$$\frac{\partial \rho \varepsilon}{\partial t} + \frac{\partial (\rho u_i \varepsilon)}{\partial x_i} = \frac{\partial}{\partial x_j} \left(\frac{\mu + \mu_t}{P_{r_\varepsilon}} \frac{\partial \varepsilon}{\partial x_j} \right) + C_{\varepsilon 3} \rho \varepsilon \frac{\partial u_i}{\partial x_i} + \left(C_{\varepsilon 1} \frac{\partial u_i}{\partial x_j} \tau_{ij} - C_{\varepsilon 2} \rho \varepsilon + C_S S_S \right) \frac{\varepsilon}{k} + S - \rho R \tag{11}$$

Where, u_i represent flow variables (e.g., velocity). τ_{ij} *is* the Reynolds stress. μ_t is the turbulent viscosity. *Pr* is the Prandtl constant. *S* is the user-supplied source term and S_s is the source term that represents interactions with discrete phase (spray). The $C_{\varepsilon i}$ terms are model constants that account for compression and expansion.

2.2 Calculation Flowchart
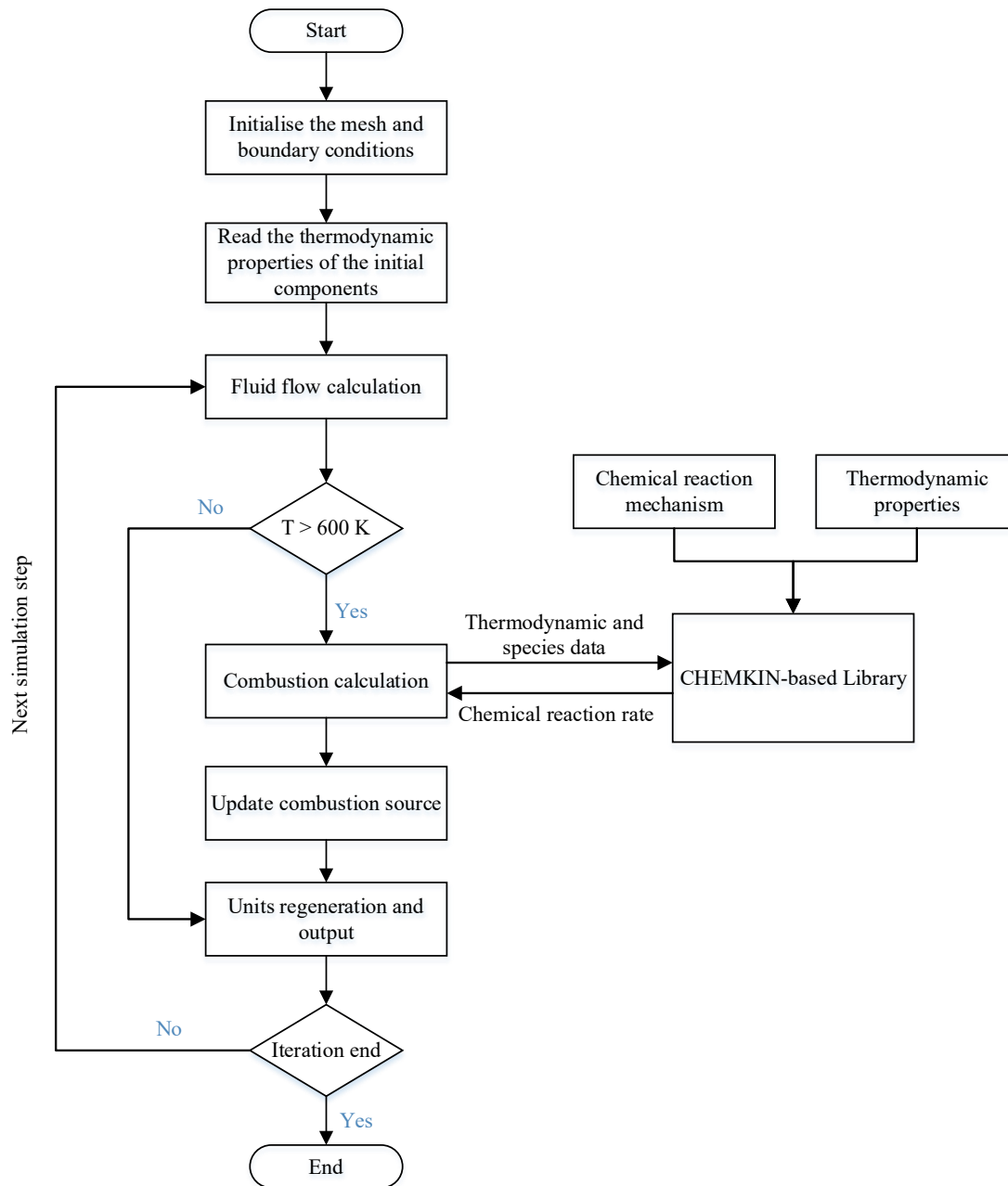
Figure 1 Calculation flowchart of the developed 3D CFD model in CONVERGE

Figure 1 shows the calculation flowchart of the 3D CFD simulation model developed in the CONVEGE

software. As seen from Figure 1, the calculation starts with the initialisation of the mesh and boundary

conditions, then the thermodynamic properties of the initial species are loaded. After completing the fluid

field calculation, the temperature is used to determine whether the combustion starts. In the present study,

when the calculated temperature gets higher than the threshold value (600 K), the physical fluid process

starts to couple with the chemical reaction process. The thermodynamic and species data are transferred

to the CHEMKIN-based library, which returns the chemical reaction rates. After the combustion resource

is updated, there will be the mesh regeneration and results output. When the calculated temperature is

lower than 600 K, the calculation flow jumps directly to the mesh regeneration and results output. If the

iteration is not yet finished, the calculation flow returns to the fluid flow calculation at next simulation

step, otherwise the calculation flow ends.

3. Model Setup and Validation

3.1 Engine characteristics and experiment setup

The investigated YC6K dual fuel engine was converted from a YC6K diesel engine by adding a natural

gas supply system and updating its Electronic Control Unit (ECU). It operates in two different modes,

the diesel mode and dual-fuel mode. Diesel fuel with lower auto-ignition temperature serves as an

ignition source for the natural gas combustion. The diesel fuel contributes to around 10% of the total

energy release in dual-fuel mode at the nominal working condition. The main characteristics of the YC6K

dual-fuel engine are shown in Table 2.

Table 2 YC6K DF engine main characteristics

Parameter	Unit	
Bore	mm	129
Stroke	mm	155
Nominal Engine Speed	rpm	1800
Nominal power per cylinder	kW	65
Compression Ratio	-	16.5:1
Inlet valve close	°CA, ABDC	2
Exhaust valve open	°CA, BBDC	31

The experimentally measured parameters for the investigated engine include in-cylinder pressure, fuel

mass flow rate, inlet air mass flow rate, inlet/exhaust manifold pressure and emissions. Heat release rate

(HRR) is calculated based on the measured in-cylinder pressure. The technical specifications of the

employed sensors have been reported in the author's previous publication [57], as shown in Table 3. As

seen from Table 3, the uncertainties of the employed sensors are within the acceptable range. In addition,

the measurement of each parameter was repeated three times for reducing the measurement uncertainty

by selecting the experimental result with smallest standard deviation.

Table 3 Employed sensors specifications [57]

Equipment	Type	Measured Error/ Uncertainty/Linearity
In-cylinder pressure sensor	AVL GU22CK [58]	$\le \pm 0.3\%$
Combustion analyser	KiBox To Go 2893 [59]	Approx. 5 ms ($\ll$ 1 combustion cycle)
Diesel consumption meter	AVL 735C [60]	$\le 0.12\%$
Gas consumption meter	E+H 83F25-XRW2/0 [61]	$\le \pm 0.05$
Air-mass flow meter	ABB FMT 700 [62]	$\le 0.8\%$
Exhaust pressure sensor	AVL LP11DA [63]	$\le \pm 0.1\%$
Emission analyser	AVL AMA i60 R1 [64]	$\le \pm 2\%$

A natural gas chromatographic analyser [65] is used to measure the composition of the employed

compressed natural gas (CNG), which consists of CH_4 (86.37% in volume fraction), CH_4 (3.67%), C_3H_8

(0.02%), n-C_4H_{10} (0.01%), CO_2 (4.70%), N_2 (2.55%) and CO (2.68%). The Lower Heating Value (LHV)

of the employed natural gas is 47.18 MJ/kg. The diesel fuel used in the DF engine testing was the light

fuel of grade No. 0 [66]. The diesel LHV is 42.652 MJ/kg, whilst its Cetane Number is 50. Table 4 shows

the operating parameters under six working conditions considering the propeller characteristic curve [67].

Table 4 Operating parameters under six conditions on the propeller curve

Operation load	%	32	42	53	74	85	100
Power	kW	95	127	159	222	254	300
Rotational speed	rpm	1228	1352	1457	1629	1703	1800
Intake manifold pressure	bar	1.48	1.79	2.11	2.69	2.80	2.91
Intake manifold temperature	°C	24	26	29	35	37	38
Pilot injection timing	°CA	−5	−5	−5	−5	−5	−5
Maximum pilot injection pressure	bar	800	800	800	800	800	800
Pilot diesel mass flow rate	kg/h	3.75	4.15	4.62	5.33	5.58	5.91
Natural gas mass flow rate	kg/h	17.89	25.53	32.90	47.89	53.03	59.47
Air mass flow	kg/h	659	860	1098	1542	1664	1783

3.2 Model setup

The combustion chamber geometry of the investigated DF engine was modelled by using the *Make*

engine sector surface tool which is embedded in the CONVERGE software. As the eight nozzle orifices are evenly spaced around the pilot injector, a 45°CA sector mesh of the combustion chamber was used to model one spray plume to take advantage of the axial symmetry. The computational domain at the TDC is shown in Figure 2. The mesh document in "CVG.in" format was then imported to the CONVERGE studio, which was used to set the initial conditions, boundary conditions, spray model, combustion model and emissions model. The simulation duration of the developed 3D CFD model is from the inlet valve closure (IVC) to exhaust valve open (EVO).
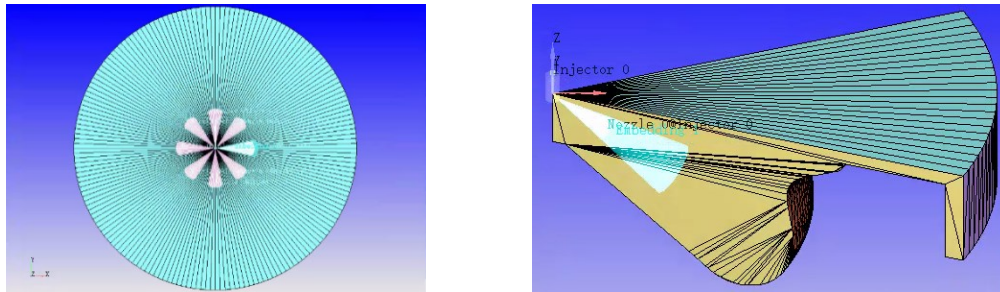
Figure 2 Computational domain of complete and one-eighth of the combustion chamber at TDC

3.3 Computation mesh study

CONVERGE provides a mesh control strategy with base grid size, adaptive mesh refinement (AMR) and fixed mesh refinement. The details of employed mesh control strategy are shown in

Table 5. In the present study, the maximum embedding level and sub grid criterion of velocity adaptive mesh refinement were set to 2 and 2.0 m/s, respectively. The maximum embedding level and sub grid criterion of temperature adaptive mesh refinement was set to 2 and 5.0 K, respectively. The fixed refinement scale of the nozzle was set to 2, while those of the piston and head were set to 1. For all the mesh refinement except for the nozzle, the refinement durations were from –20°CA to 129°CA in order to cover the combustion period. However, the duration of the nozzles mesh refinement was set from –5° CA to 10°CA, which corresponds to the pilot injection duration of the baseline case. When investigating the effects of pilot injection timing in the following study, the duration of the nozzles mesh refinement

15

needs to be adjusted according to the actual injection timing.

Table 5 Mesh control strategy

Base grid size	1.5mm, 2.0mm, 2.5mm, 3.0mm			
Adaptive mesh refinement		Max embedding level	Sub-grid criterion	Duration
	Velocity	2	2.0 m/s	–20°CA to 129°CA
	Temperature	2	5.0 K	–20°CA to 129°CA
Fixed mesh refinement		Scale	Embed layers	Duration
	Nozzles	2	–	–5°CA to 10°CA
	Piston	1	1	–20°CA to 129°CA
	head	1	1	–20°CA to 129°CA
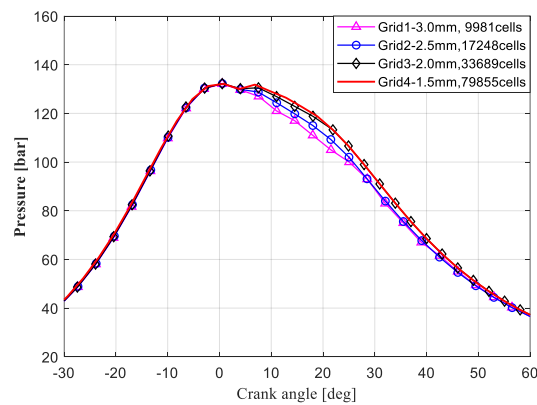
Figure 3 In-cylinder pressure comparison with four mesh sizes

The base grid size affects the computation speed and prediction accuracy of CFD models. In order to

exclude the influence by the mesh grid size, a comparison of in-cylinder pressure with four grid sizes at

the nominal operating condition is conducted to check the mesh grid size independence, as presented in

Figure 3. The pressure curve of grid 3 is remarkably consistent with that of grid 4, but differs from that

of grid 1 and grid 2. Balancing the computation cost and prediction accuracy, grid 3 of 2 mm basic grid

size and 33689 basic cells would be the best choice for the following CFD modelling.

3.4 Knocking detection setup

In order to detect potential knocking occurrence inside the combustion chamber, seven monitoring points

were evenly placed at the XY plane to monitor the local pressure oscillation, as shown in Figure 4.

Considering knocking phenomenon is usually caused by spontaneous combustion in the unburnt zone

16

before flame front arrives [20], knocking is not likely to occur around the piston bowl because the spray

penetration of pilot diesel almost reaches the longest distance of piston bowl. The seven monitoring

points were placed near the cylinder head (points P1-P4) and liner (points P5-P7) [14, 68], which are

away from the pilot diesel spray and thus are prone to auto-ignition before being approached by the flame

front.
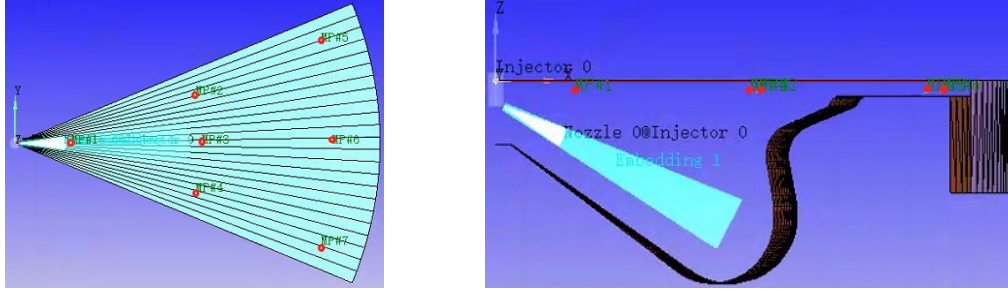
Figure 4 Locations of the local pressure monitoring points

The knock index (KI) was introduced to define the intensity of knock [69] to quantify the knock

phenomenon. The definition of KI is according to Eq (12).

$$KI = \frac{1}{N}\sum_{1}^{N} PP_{max,n}$$

(12)

Where, $PP_{max,n}$ is the largest absolute difference of the band-pass (5 kHz ~ 20 kHz) filtered pressure [70]

at position n.

3.5 Model validation

The in-cylinder pressure, heat release rate and emissions (NOx, CO and HC) at four operating conditions

on the propeller characteristic were obtained for validating the accuracy of the developed 3D CFD model.

The measure in-cylinder pressure signals include noise due to the inherent character of the combustion

process. Thus, the method proposed in reference [71] was employed to first smooth the pressure signal

and subsequently average 200 cycles; the latter was employed for the developed model validation.

17

(a) 100% load: 300 kW, 1800 r/min

(b) 74% load: 222 kW, 1629 r/min

(c) 53% load: 159 kW, 1457 r/min

(d) 32% load: 95 kW, 1228 r/min
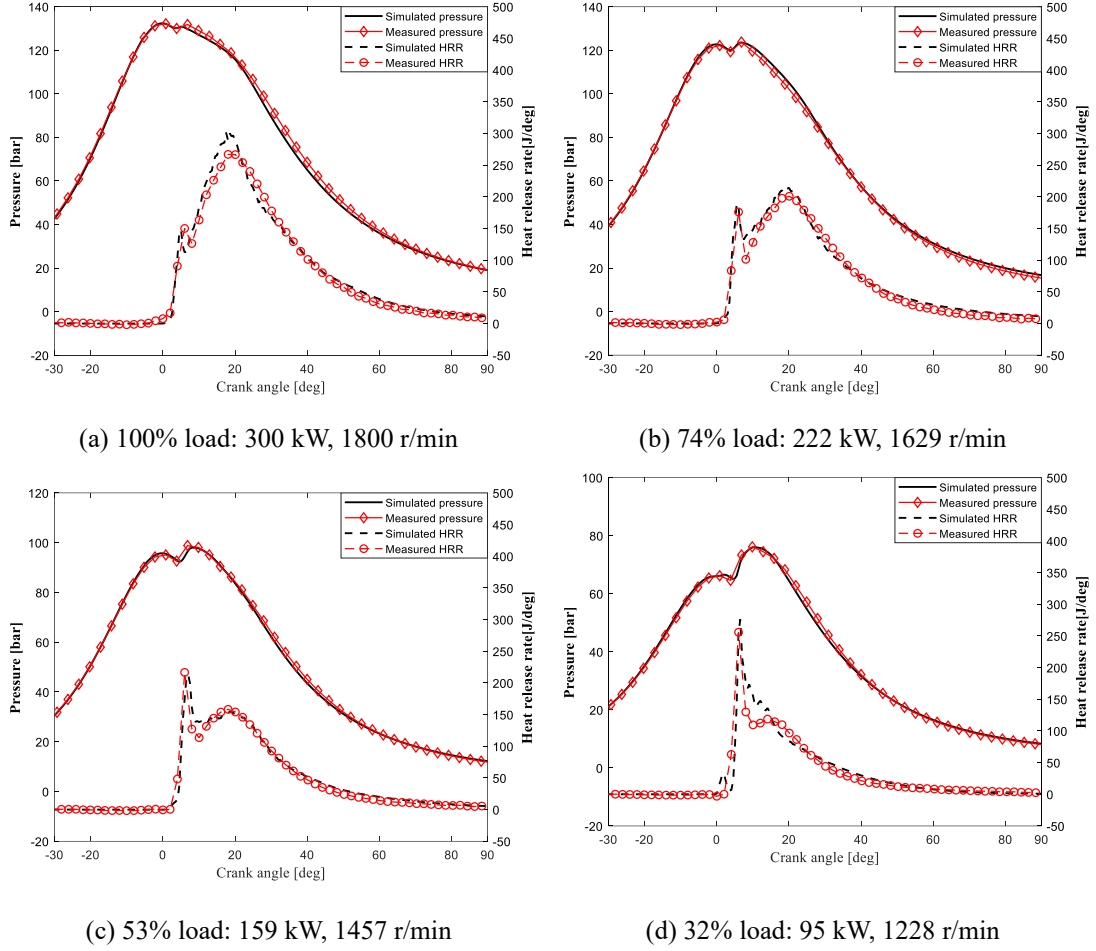
Figure 5 Simulated and measured in-cylinder pressure and heat release rate of the investigated engine at different operating loads: (a) 100%; (b) 74%; (c) 53%; (d) 32%.

Table 6 Quantitative Comparison between the simulated and measured in-cylinder pressure and heat release rate at different operating loads: (a) 100%; (b) 74%; (c) 53%; (d) 32%.

Operating loads	Parameters	p_{max}	α_1	IMEP	HRR_{max}	α_2	Accumulated HRR
	Unit	bar	°CA	bar	J/°CA	°CA	J
100% load: 300 kW, 1800 r/min	Simulation	134.31	0.00	19.20	299.88	18.56	9132.6
	Experiment	132.36	0.20	18.90	278.56	18.09	8645.6
	Error (% or °CA)	1.47	0.20	1.59	7.65	0.47	5.63
74% load: 222 kW, 1629 r/min	Simulation	124.54	6.53	18.50	214.07	20.01	6954.0
	Experiment	123.80	6.23	18.00	200.79	20.10	6509.4
	Error (% or °CA)	0.06	0.30	2.78	6.61	0.09	6.83
53% load: 159 kW, 1457 r/min	Simulation	97.95	8.02	12.00	216.65	6.03	5387.4
	Experiment	98.84	6.83	12.30	212.74	7.03	5055.3
	Error (% or °CA)	0.90	1.19	2.44	1.84	1.00	6.57
32% load: 95 kW, 1228 r/min	Simulation	76.05	7.30	9.80	276.02	6.51	3746.6
	Experiment	74.81	9.49	9.70	255.76	6.03	3522.9
	Error (% or °CA)	1.66	2.19	1.03	7.92	0.48	6.35

Figure 5 shows the comparison of the simulated and measured in-cylinder pressure and heat release rate

(HRR) at four different operating conditions. The quantitative comparisons of maximum pressure (p_{max})

and its corresponding crank angle (α_1), IMEP, maximum HRR (HRR_{max}) and its corresponding crank

angle (α_2), and accumulated HRR are shown in Table 6. The relative errors of p_{max} and IMEP are below

3%, whilst the relative errors of maximum HRR and accumulated HRR are within 8%. In addition, the

absolute differences of the maximum pressure and HRR are less than 3°CA. As can be deduced from

Figure 5 and Table 6, the simulated results demonstrate adequate agreement with the measured data,

which proves that the developed 3D CFD model is capable of effectively representing the engine

performance with adequate accuracy. However, the peak values and accumulated values of the simulated

HRR are slightly higher than those of the HRR calculated from the measured in-cylinder pressure, which

is attributed by the following reasons: (1) all the cells are considered as prefect mixing zones in the 3D

CFD model, resulting in faster combustion speed of homogeneous charge, whilst the actual mixture is

usually inhomogeneous; (2) the boundary conditions set in the 3D CFD model, including the cylinder

head temperature, liner temperature and piston temperature, do not coincide with those parameters actual

values.

The comparisons of the simulated and measured emissions (NOx, CO and HC) are presented in Table 7.

All the relative errors between the simulation result and measured data are less than 10% except those of

HC emission at 74%, 53% and 32% loads. It is attributed to the over estimation of the in-cylinder

temperature at these three operating conditions, which can be inferred from the fact that the simulated

NOx emissions are higher than the measured NOx emissions. In addition, the methane slip during gas

exchange is not considered in the 3D CFD model, resulting in underestimation of the HC emissions.

However, considering the preceding factors, the developed model emissions prediction capability is

deemed acceptable.

Table 7 Comparison between the simulated and the measured emissions parameters.

Operating loads	Parameters Unit	NOx g/(kWh)	CO g/(kWh)	HC g/(kWh)
100% load: 300 kW, 1800 r/min	Measurement	1.83	6.82	17.67
	Simulation	1.67	7.47	18.80
	Relative error (%)	8.74	9.53	6.40
74% load: 222 kW, 1629 r/min	Measurement	1.34	9.36	32.45
	Simulation	1.47	8.55	28.40
	Relative error (%)	9.70	8.65	12.48
53% load: 159 kW, 1457 r/min	Measurement	1.50	7.21	24.93
	Simulation	1.62	6.50	22.30
	Relative error (%)	8.80	9.85	10.55
32% load: 95 kW, 1228 r/min	Measurement	1.62	3.77	10.30
	Simulation	1.70	3.45	8.90
	Relative error (%)	4.94	8.49	13.59

It's worth mentioning that in order to obtain an accurate CFD model, the spray model usually needs to

be calibrated by using image based experiment data [72, 73] like spray penetration, liquid length, vapor

penetration, etc. But, the spray model in this study is not calibrated because the aforementioned

experiment data is not available. However, the detailed injector geometry and measured injection

parameters (pressure, duration, profile, mass) are provided, which help refine the spray model with

sufficient input parameters. As the simulated diesel spray exhibits enough penetration distance without

hitting the combustion chamber, the spray model is considered as qualitatively calibrated. In addition,

the comparison with the experimentally obtained pressure, HRR and emissions proves the developed

CFD model is with sufficient accuracy.

4. Parametric Investigation on Engine Operating Settings

The validated CFD model is used to investigate the effects of selected settings on the engine performance,

emissions and knocking occurrence at three operating loads (100%, 74% and 53%). However, for brevity

reasons, only the results at 100% operating load are presented herein. In addition, parametric runs at the

three operating loads are performed to explore the potential engine settings that could provide a simultaneous reduction of BSFC and NOx emissions whilst avoiding knocking occurrence.

The pilot injection timing, equivalence ratio and natural gas mass are selected for an effect investigation on the engine performance, emissions and knocking occurrence of the investigated dual fuel engine. As the NG-air mixture is ignited by the pilot diesel, the pilot injection timing plays an important role in determining the start of combustion and the following combustion process [74], thus affecting the engine performance and emissions significantly. The air-fuel equivalence ratio (λ) proves to be an influencing factor for DF engine combustion characteristics including peak heat release and combustion duration, which subsequently affect the BSFC and emissions [75]. Natural gas mass, which has a direct impact on the input energy, NG-diesel mass ratio and in-cylinder gas properties [76, 77], are also included in this investigation.

The variation levels of selected engine operating settings for individual effect investigation are presented in Table 8. The pilot injection timing, equivalence ratio and natural gas mass of baseline case (100% load) are –5°CA ATDC, 1.62 and 59.47 kg/h, respectively. Since the pilot injection timing at baseline case is –5°CA ATDC, the variation levels of pilot injection timing in Table 8 are set in advance to the baseline case (–15°, –12.5°, –10°, –7.5° and –5° ATDC) rather than equally distributed around the baseline case to avoid injection starting after the TDC. The effect of each influencing factor is individually investigated, keeping the values of other two factors at their baseline values.

Table 8 Investigates engine settings at 100% load

Operating settings	Units	Levels				
Pilot injection timing	°CA	–15	–12.5	–10	–7.5	–5
Equivalence ratio variation	%	–10	–5	0	5	10
Natural gas mass variation	%	–10	–5	0	5	10

4.1 Effects of pilot injection timing

The derived simulation results with several pilot injection timings are shown in Figure 6. As inferred

from Figure 6 (a) and (b), the maximum in-cylinder pressure, peak heat release rate (HRR) and the maximum average temperature increase with the advance of pilot injection timing. An abnormal sharp jump is spotted at the HRR curve for the case of –15°CA pilot injection timing, which implies a potential knocking occurrence around 14°CA ATDC. The mass fraction variation of CH_2O radicals with different pilot injection timing is shown in Figure 6 (c). The production and consumption rate of CH_2O radical affects the low-temperature reaction regime of methane [14]. As the CH_2O radical is mainly distributed in front of the flame, it can be used as the precursor of oxidation reaction in dual fuel engines [78]. With the pilot injection timing advance, the CH_2O radicals formation starts advanced with an increasing production rate. The above-mentioned abnormal sharp jump for the case of –15°CA pilot injection timing can also be observed in the mass fraction of CH_2O radicals, from which it can be inferred that the spontaneous combustion of methane caused a knocking combustion. The details (location and timing) of the knocking occurrence are discussed in the following paragraphs.

Figure 6 (d) demonstrates that the Knock Index slightly increases from –5°CA to –12.5°CA whereas a sheer increase is observed at –15°CA, implying a knocking occurrence. Similar results were reported by Yang [79] that the combustion noise is obviously deteriorated with the advanced pilot injection timing of a diesel/natural gas dual fuel engine. The peak pressure rises above its limit (200 bar) at the pilot injection timing of –12.5 °CA and –15 °CA, which might cause severe damage to the cylinder structure and should be avoided by setting the pilot injection timing after –12.5°CA. Figure 6 (e) shows that the BSFC decreases with the pilot injection advance, whereas the IMEP exhibits the contrary trend. The early injection of the pilot diesel increases the air-fuel mixing duration, which results in a higher concentration of the chemical reactive combustible mixture during the injection delay period. Once the combustion starts, more ignition spots and faster flame propagation speed occur, leading to higher combustion

22

efficiency, thus lowering the BSFC.

(a) In-cylinder pressure and heat release rate

(b) In-cylinder temperature

(c) CH$_2$O mass fraction

(d) Knock index and peak pressure

(e) IMEP and BSFC
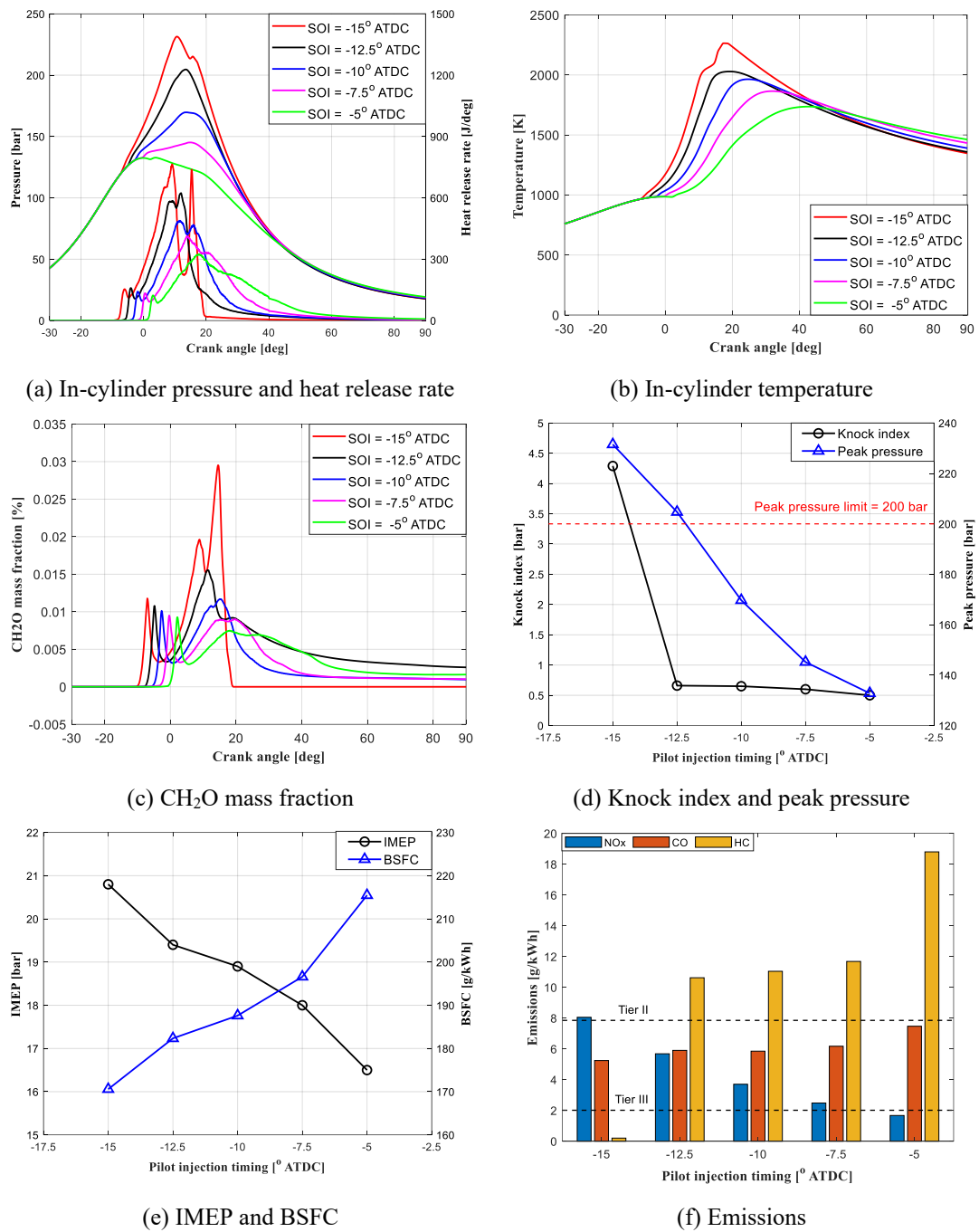
(f) Emissions

Figure 6 Simulation results with pilot injection timing variation

However, higher combustion efficiency is associated with higher in-cylinder temperature, which results in increasing NOx emissions with the pilot injection advance. As shown in Figure 6 (f), the NOx emissions at all the cases except the baseline case stays higher than the Tier III limits, while the NOx emissions at –15°CA pilot injection even fails to meet the Tier II limits. It must be noted that the Tier

limits provide aggregated values over four operating points, hence they are employed herein as an

indicator to characterise the NOx emissions. The HC and CO emissions exhibit a decreasing trend with

the advance of pilot injection timing, which can also be attributed to the higher combustion efficiency.

For further delineating the in-cylinder combustion process, the distributions of in-cylinder temperature

with different starts of injection (SOI) are presented in Figure 7. The temperature profile provides a visual

representation of the location of the high-temperature regions inside the combustion chamber, which is

important for the analysis of the NOx emissions. As inferred from Figure 7, the advanced pilot injection

timing results in larger high-temperature areas, which justifies the NOx emissions increase (Figure 6 (f)).
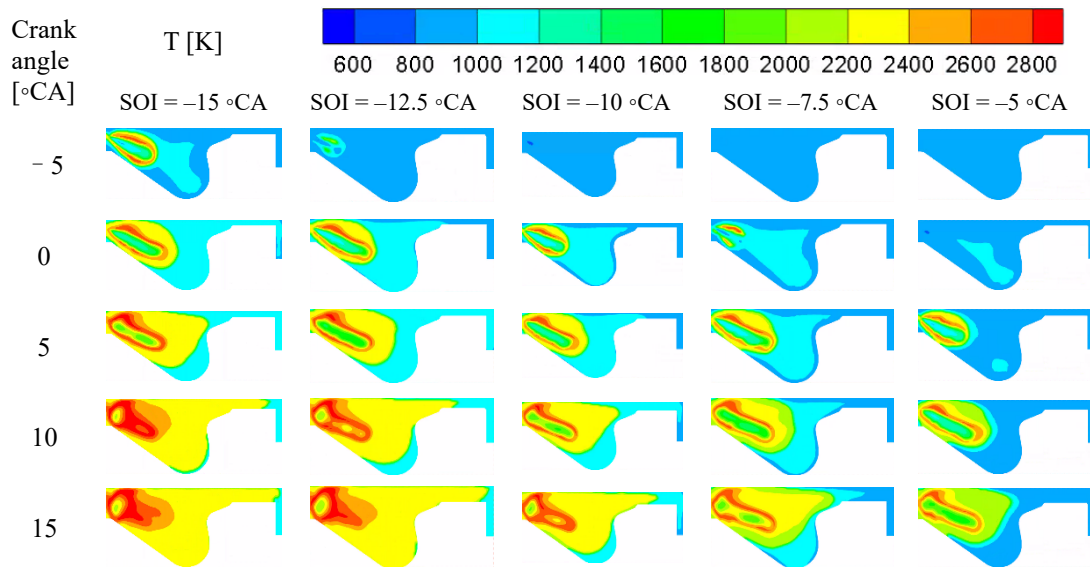
Figure 7 In-cylinder temperature distribution with pilot injection timing variation

The distributions of CH_2O radical are shown in Figure 8, where the grey area denotes the 1800 K

temperature contour representing the flame front. At the ignition stage, high concentration of CH_2O

radical was spotted in the pilot spray zone, as a portion of CH_4-air mixture was entrained into the spray

zone and got involved in the low-temperature reaction of CH_4. For all the five cases presented in Figure

8, the combustion starts from the pilot diesel spray indicating that the diesel fuel with higher cetane

number (42 to 55) plays the role of ignition source for the natural gas with lower cetane number (<10).

24

Ickes [80] investigated the cetane number effects on the combustion characteristics of a dual fuel diesel engine operating with natural gas. It was found that at higher loads the dual fuel operation needs ignition fuels with cetane number higher than 45, while normal diesel operation is possible with cetane number 35 to 40 fuels. Once the flame propagation starts, the CH_2O radical was mainly distributed in front of the flame, indicating the precursor of an oxidation reaction. With the advance of the pilot injection timing, the flame propagated further inside the combustion chamber, which resulted in advanced combustion phase and faster heat release rate. It is worth mentioning that high concentration of CH_2O radical was observed in front of the flame arrival at around 15°CA for the case of –15°CA SOI, indicating a knocking occurrence and explained the high KI shown in Figure 6 (d).
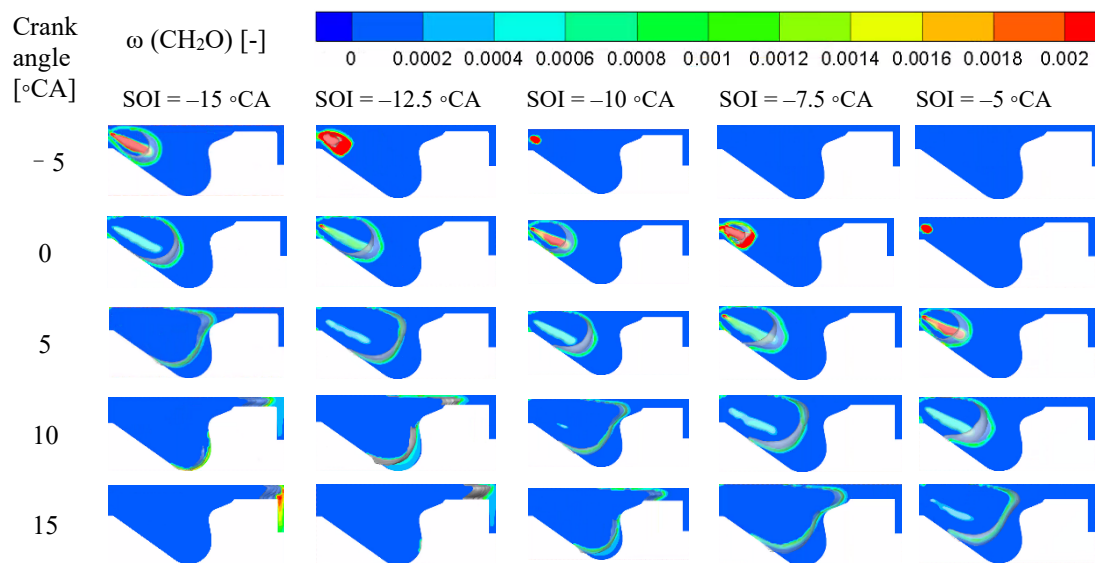
Figure 8 In-cylinder CH_2O distribution with pilot injection timing variation

4.2 Effects of equivalence ratio

Figure 9 shows the simulation results, in specific, the presented parameters are plotted against crank angle for several equivalence ratio values. As inferred from Figure 9 (a) and (b), the equivalence ratio variation increase causes the maximum in-cylinder pressure increase, which is attributed to the increased initial pressure. The peak heat release rate and the maximum average temperature reduced with the equivalence ratio increase. However, the HRR decreased with higher equivalence ratio values due to the

slower chemical reaction rate caused by the dilution effect of more fresh air. The integrated HRR with +10% equivalence ratio difference (from its baseline value) was only 84.2% of that with –10% equivalence ratio difference, implying an incomplete combustion process fro the former case. As inferred from Figure 9 (c), the increasing final value of the CH_2O mass fraction demontrates that more CH_2O radicals were left unconsumed at EVO, leading to higher HC emissions, as shown in Figure 9 (f).

(a) In-cylinder pressure and heat release rate

(b) In-cylinder temperature

(c) CH_2O mass fraction

(d) Knock index and peak pressure

(e) IMEP and BSFC

(f) Emissions
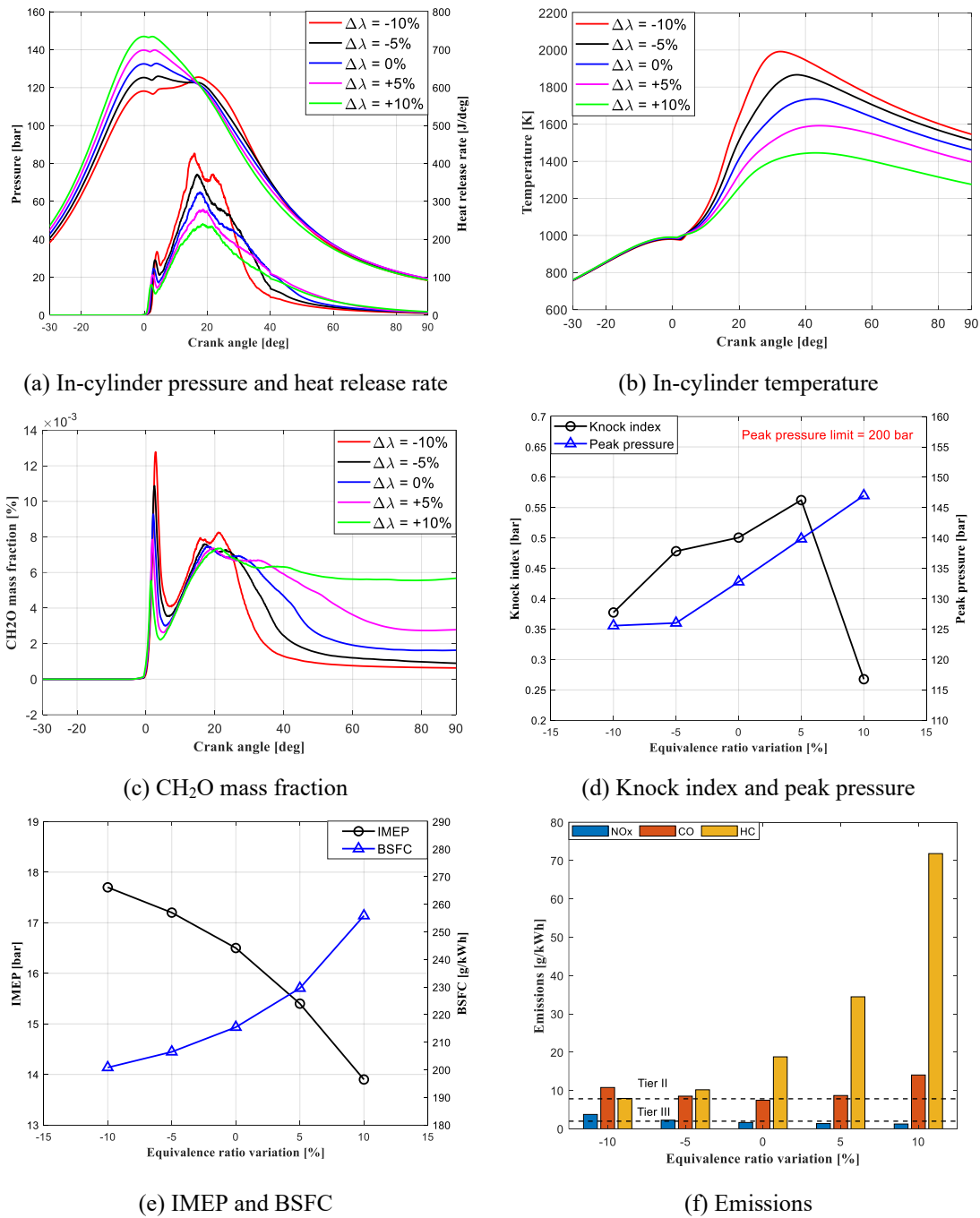
Figure 9 Simulation results with equivalence ratio variation

As illustrated in Figure 9 (d), the Knock Index (KI) exhibited higher values with the increase of the equivalence ratio, influencing the knocking phenomenon occurence. However, the KI dropped to a low level with the +10% equivalence ratio difference due to the incomplete combustion. The maximum in-cylinder pressure shows an considerable increase from 125 bar to 147 bar, whilst all the predicted maximum pressure values are well below the peak pressure limit of 200 bar. Figure 9 (e) shows a significant increase in BSFC and a decrease in IMEP, which can be explained by the slower combustion rate with the increase of equivalence ratio. The decreased peak heat release and exhaust gas temperature as well as increased BSFC with larger air-fuel equivalence ratio (λ) were supported by Zheng [75]. It's worthing mentioning that the results are presented versus air-fuel equivalence ratio (λ) in this study whilst the fuel-air equivalence ratio (φ) is used in Zheng's work [75]. In Figure 9 (f), the NOx emissions reduced by increasing the equivalence ratio and started to meet with the Tier III regulations when the equivalence ratio above its baseline value. The HC emissions exhibited a contrary trend to the NOx emissions, whilst the HC emissions achieved its lowest level at –10% equivalence ratio variation from its baseline value.
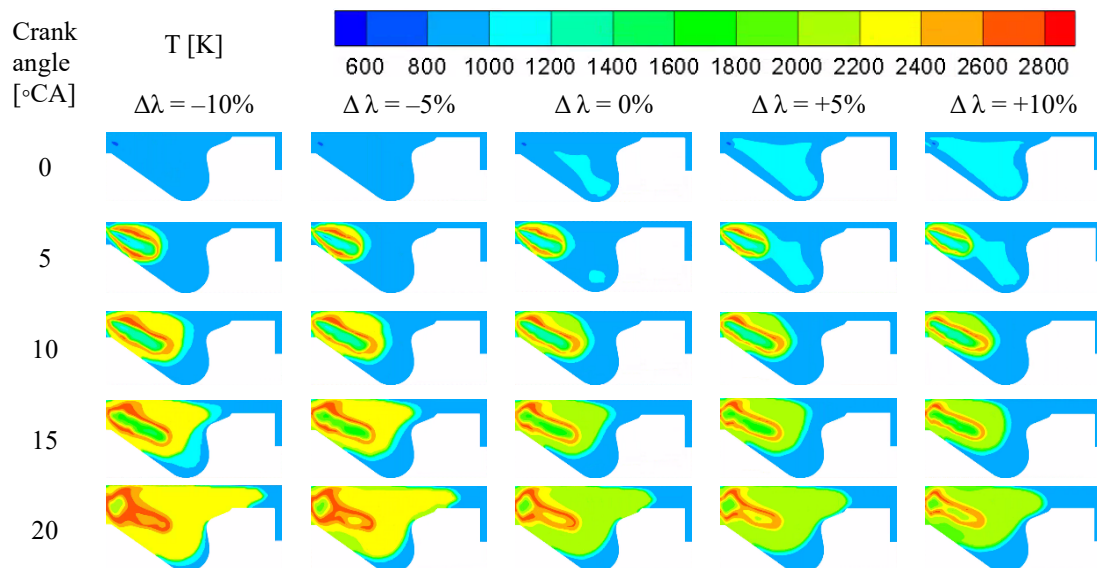
Figure 10 In-cylinder temperature distributions with equivalence ratio variation

Figure 10 presents the distributions of the in-cylinder temperature with the equivalence ratio variation.

With higher equivalence ratio values, the compression pressure at TDC (0∘CA) increases causing a larger

high-temperature region (between 1000 K and 1200 K). However, larger equivalence ratio caused leaner

air-fuel mixture, resulting in slower combustion speed. Thus, smaller area of high-temperature region

(between 2000 K and 2800 K) was spotted after the flame starting its propagation, which explains the

NOx emissions reduction and the HC emissions increase shown in Figure 9 (f).
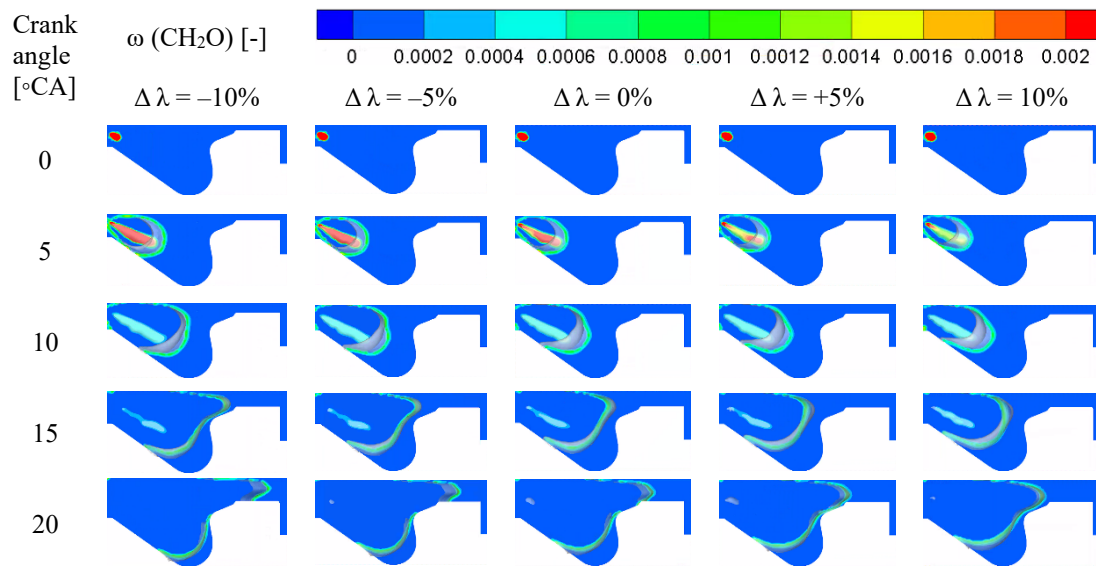
Figure 11 In-cylinder CH_2O distribution swith equivalence ratio variation

The distributions of CH_2O radical and 1800 K temperature contours are shown in Figure 11. As seen

from the comparison at 5∘CA, the CH_2O radical concentration inside the spray zone is much higher than

the remaining space, which means that low-temperature reaction plays dominant role inside the spray

zone. The longer flame propagation distance indicated by the 1800 K temperature contour implies that

flame propagates faster with smaller equivalence ratio.

4.3 Effects of natural gas mass

As seen from Figure 12 (a), (b) and (c), the NG mass increase did not make significant difference to the

shape of the in-cylinder pressure and the HRR, the average temperature, as well as the mass fractions of

CH_2O radicals. However, it resulted in increasing the maximum in-cylinder pressure values, attributed

to the initial cylinder pressure increase. Figure 12 (d) and (e) demonstrate that the KI and IMEP increased

with higher NG mass, whilst the BSFC was reduced from 220 g/(kWh) to 214 g/(kWh), attributed to the

increase of the compression pressure and maximum in-cylinder pressure. Figure 12 (f) demonstrates that

the emissions of NOx, HC and CO slightly reduce with increasing the NG mass. In addition, the NOx

emissions at all the investigated cases were well below the Tier III limit. It must be noted that the

simultaneous reduction of BSFC and emissions is achieved when the NG mass increased.

(a) In-cylinder pressure and heat release rate

(b) In-cylinder temperature

(c) CH$_2$O mass fraction

(d) Knock index and peak pressure

(e) IMEP and BSFC

(f) Emissions
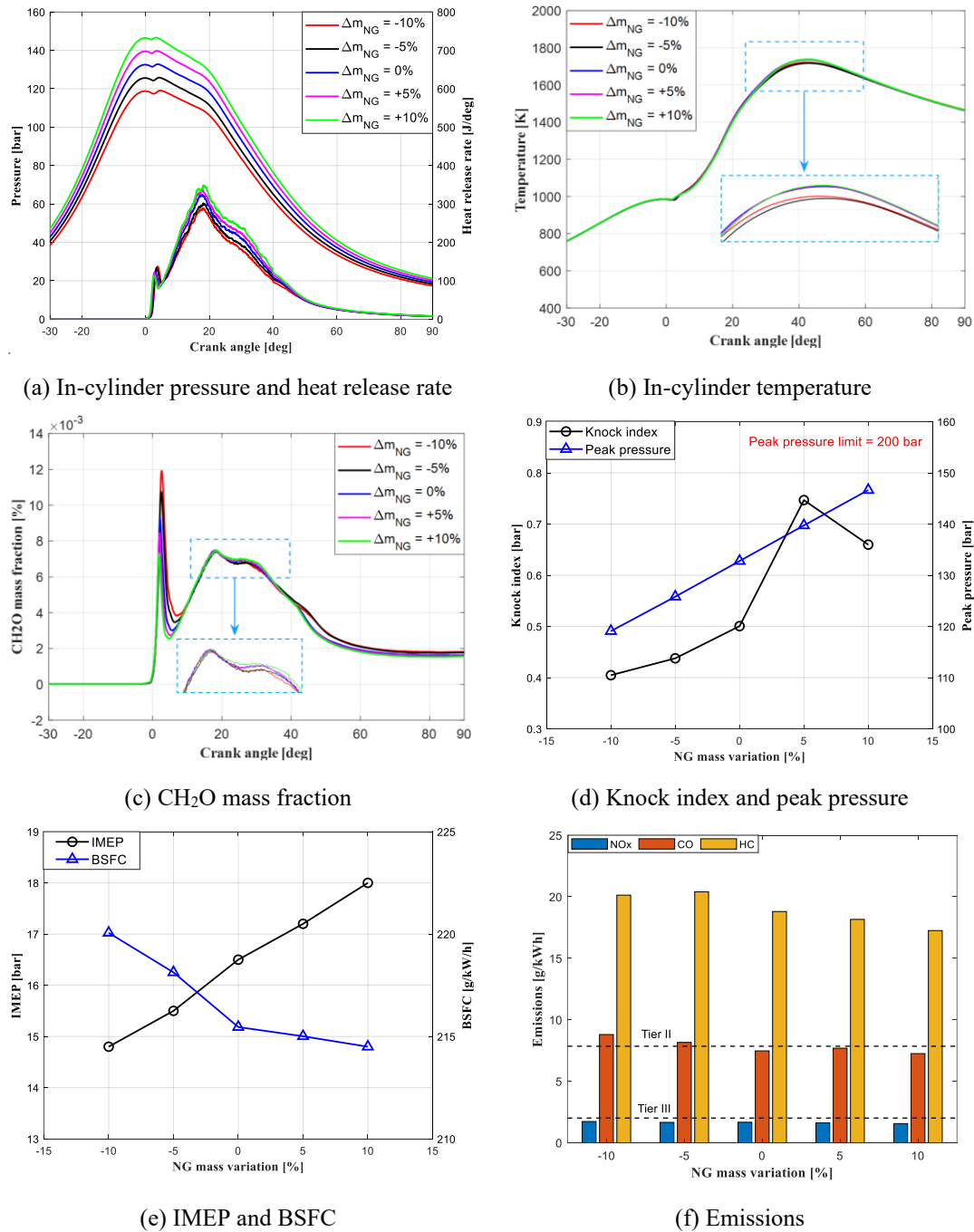
Figure 12 Simulation results with the NG mass variation

Figure 13 presents the in-cylinder temperature distributions with the NG mass variation. When the NG mass increases, a larger area of high-temperature zone (between 1000 K and 1200 K) was spotted at the TDC (0∘CA), which is caused by the increasing initial pressure. However, after the flame propagation starts at around 5∘CA, the NG mass variation does not show an apparent effect on the in-cylinder temperature distribution, which is in accordance with the result indicated by the HRR presented in Figure 12 (a).
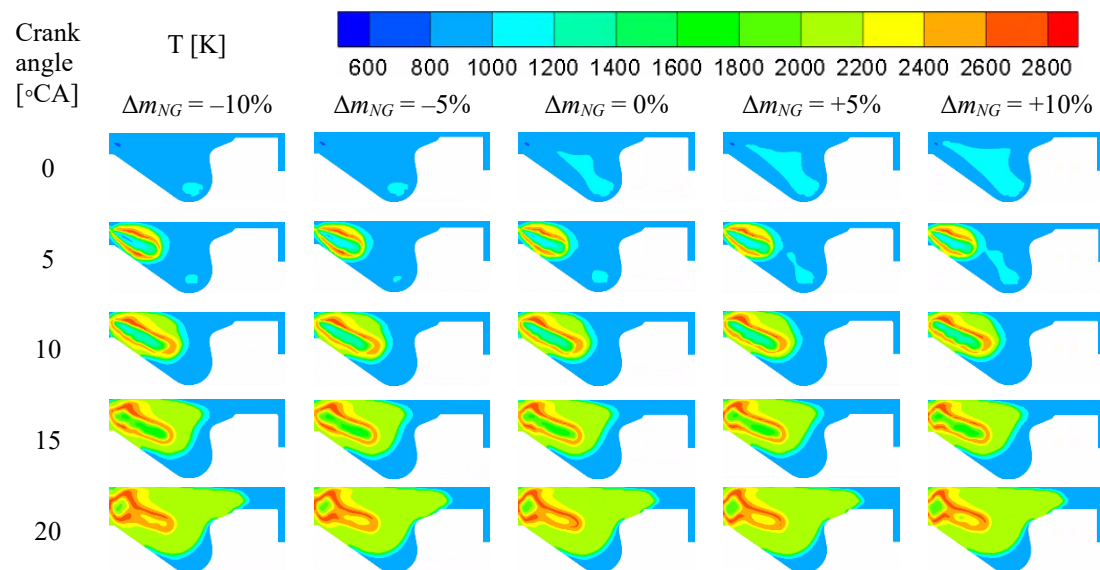
Figure 13 In-cylinder temperature distribution with different NG mass variations
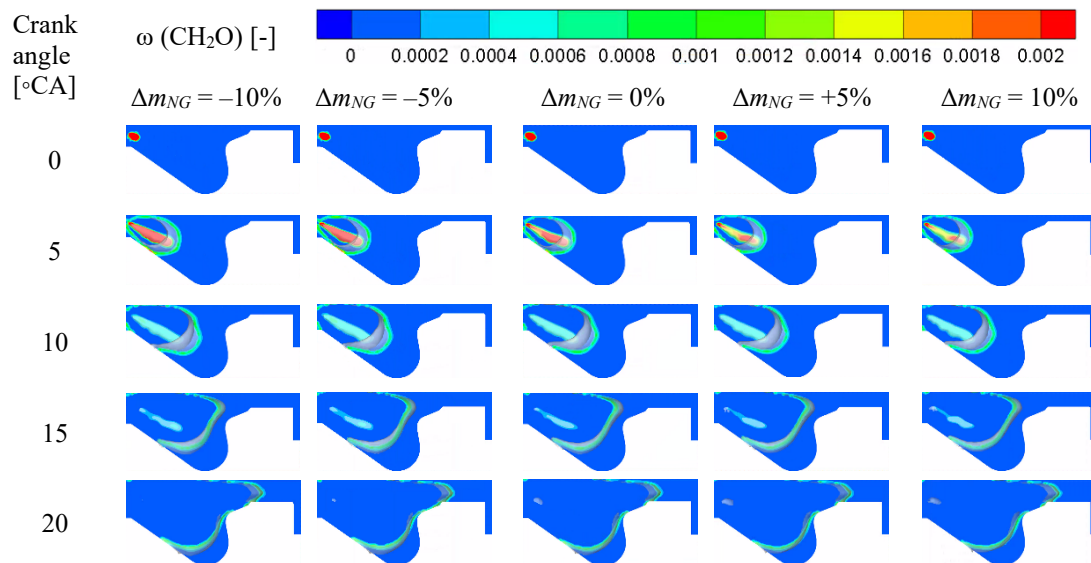
Figure 14 In-cylinder CH$_2$O distribution with different NG mass variations

The distributions of CH$_2$O radical with the NG mass variation are shown in Figure 14, where the grey

area denotes the 1800 K temperature contour representing the flame front. At the initial flame propagation stage around 5∘CA ATDC, higher concentration of CH_2O radical was spotted with smaller NG mass, which indicates more CH_4 getting involved in the low-temperature reaction and justifies the higher first peak HRR shown in Figure 12 (a). For the following flame propagation process, the NG mass variation does not make visible difference on the CH_2O distribution.

4.4 Parametric investigation

This section reports the performed parametric study to investigate the potential for simultaneously reducing the engine NOx emissions and BSFC, as well as avoiding knocking occurrence, by considering the following engine seettings: pilot injection timing, equivalence ratio and injected natural gas mass. Prior to conducting this parametric study, the performance-emissions trade-off at 100%, 74% and 53% loads was analysed to determine the ranges of the three selected engine settings. It must be noted that the NG mass variation causes an inevitable change to the engine output power, which implies that the engine load cannot be retained at the above-mentioned values (100%, 74% and 53%). Thus, the corresponding constant rotational speeds 1800 r/min, 1629 r/min and 1457 r/min are used herein, instead of the respective loads. The NOx-BSFC trend was also analysed to determine the variation ranges of the investigated engine settings at the selected engine speeds, considering the optimal NOx-BSFC area with BSFC values less than the baseline case and the NOx emissions meeting the Tier III requirements.

Figure 15 presents the derived simulations results of the NOx emissions versus BSFC with different settings at 1800 r/min, 1629 r/min and 1457 r/min, which were derived by employing the validated models of 100%, 74% and 53% loads, respectively. Figure 15 (a) demostrates that the NOx emissions increased with advanced pilot injection timing and reduced equivalence ratio at 1800 r/min, whilst the BSFC exhibits the contrary trend compared to NOx emissions. In addition, the predicted NOx emissions

are higher than Tier III limit when the pilot injection timing is advanced beyond –7.5°CA or when the equivalence ratio variation exceeds –5%. The NG mass variation from –10% to 10% (taking 0% as the baseline value) results in the simultaneous reduction of NOx emissions and BSFC, whilst retaining the NOx emissions lower than the Tier III limit. Thus, the cases of 5% and 10% NG mass variation overperform compared to the baseline case, achieving reduced BSFC and meeting Tier III limit. For the following parametric investigation, the maximum variation level of NG mass fraction could be increased to 20% because the influence of 10% NG mass fraction variation on the NOx-BSFC trend is relatively minor compared to the influence of the other two operating settings variations. As inferred from Figure 15 (a), the optimal engine operation at 1800 r/min can be achieved by controlling the variations of the investigated settings within the following ranges: –5 to –7.5°CA for the pilot injection timing, –5% to +5% for the equivalence ratio, and 0% to +20% for the NG mass.

The NOx-BSFC trends at 1629 r/min and 1457 r/min are shown in Figure 15 (b) and Figure 15 (c), respectively. In order to reduce the computational cost of CFD simulation cases, three levels rather than five levels of each setting are investigated. As inferred from Figure 15 (b), the optimal area at 1629 r/min can be achieved by controlling operating settings variation within the same ranges as in the case of 1800 r/min. Figure 15 (c) illustrates the trade-off between the NOx emissions and BSFC at 1457 r/min when NG mass varies from 0% to 20%, which differentiates from the simultaneous reduction of NOx emissions and BSFC at 1800 r/min and 1629 r/min. The derived CFD results at 1457 r/min indicate that the BSFC considerably increases with the increase of NG mass. Thus, the –10% variation level of NG mass is additionally investigated to explore the operating settings ranges achieving the optimal area at 1457 r/min. As inferred from Figure 15 (c), the optimal area at 1457 r/min operation condition could be obtained by setting the pilot injection timing, equivalence ratio variation and NG mass variation within the ranges of

–5 to –7.5 °CA, –5% to +5% and –10% to +10%, respectively.

(a) 1800 r/min

(b) 1629 r/min
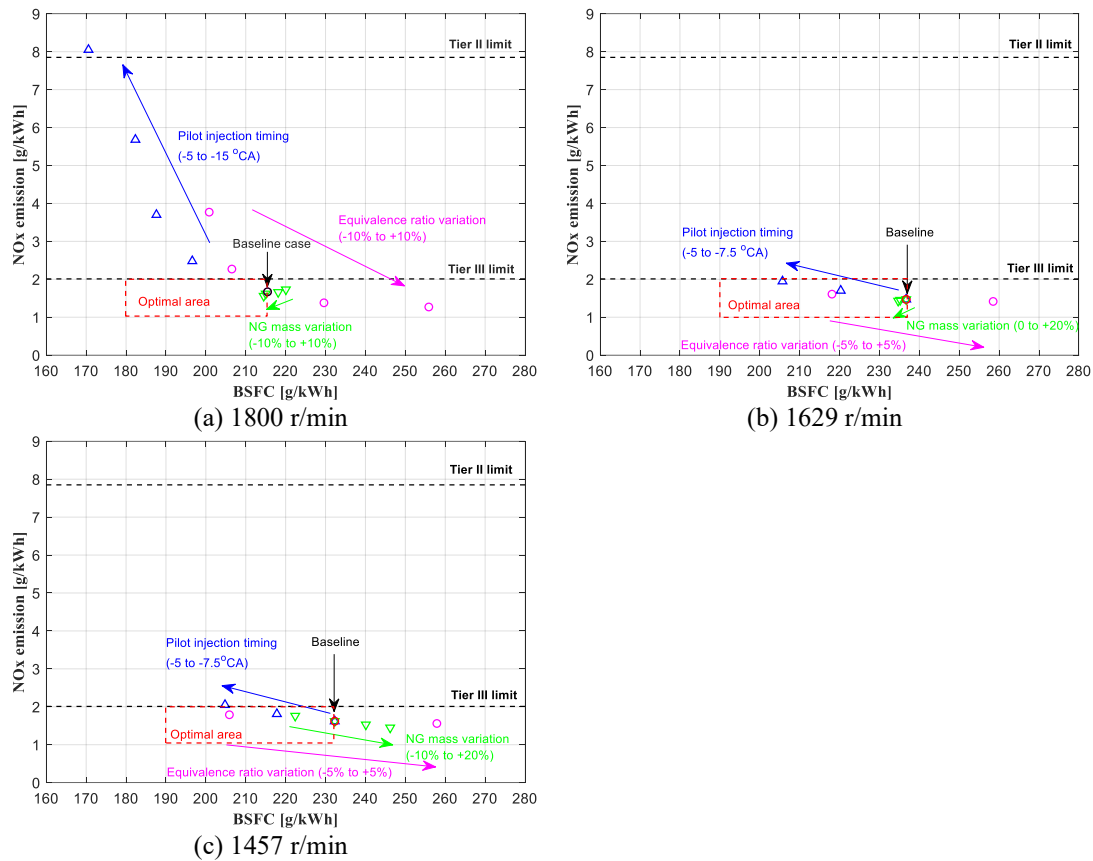
(c) 1457 r/min

Figure 15 NOx emissions versus BSFC with different operating settings at 1800 r/min (a), 1629 r/min (b), and 1457 r/min (c).

According to the preceding analysis, the level settings of the parametric investigations at 1800 r/min, 1629 r/min and 1457 r/min are listed in Table 9. The levels for the pilot injection timing and equivalence ratio variation at 1800 r/min, 1629 r/min and 1457 r/min are the following: –7.5°CA, –6.25°CA and –5°CA for the pilot injection timing, –5%, 0% and 5% for the equivalence ratio variation. The levels of NG mass variation at 1800 r/min and 1629 r/min are set to 0, 10% and 20%, whilst those at 1457 r/min are –10%, 0% and 10%. The parametric investigations are performed by using the 'full factorial' method, which generates totally 27 simulation cases. Nevertheless, not all the 27 simulation cases are actually conducted, as certain cases can be easily excluded from the optimal area by referring to the variation trend in Figure 15.

Table 9 Level settings of parametric investigations at three operation conditions

	Rotational speed (r/min)	Levels		
Pilot injection timing (°CA)	1800, 1629, 1457	A1 −7.5	A2 −6.25	A3 −5
Equivalence ratio variation (%)	1800, 1629, 1457	B1 −5	B2 0	B3 5
NG mass variation (%)	1800, 1629	C1 0	C2 10	C3 20
	1457	−10	0	10

(a) 1800 r/min

(b) 1629 r/min
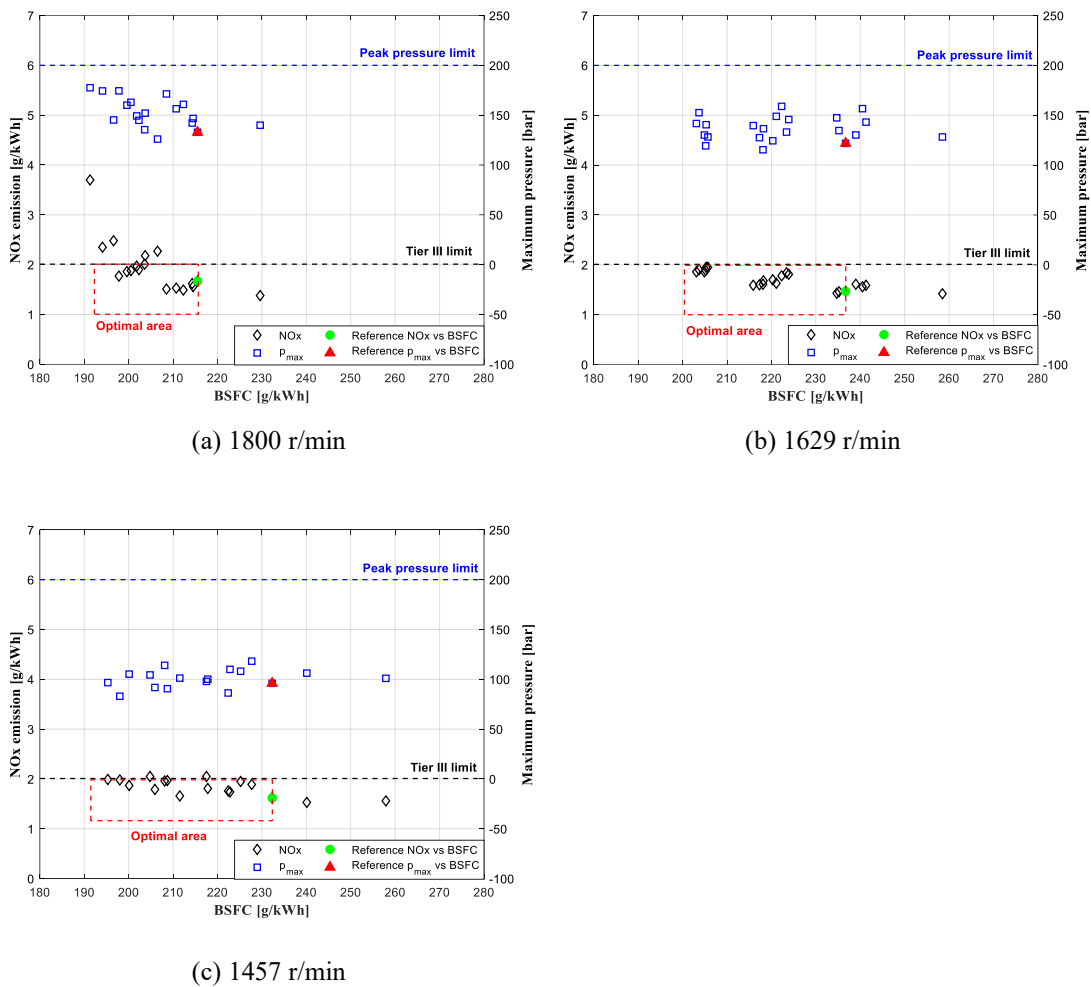
(c) 1457 r/min

Figure 16 Parametric study results showing potential for NOx emissions and BSFC reduction at 1800 r/min (a), 1629 r/min (b) and 1457 r/min (c).

Figure 16 presents the trade-off between the NOx emissions and BSFC as well as the maximum average pressure at the investigated engine speeds. As inferred from Figure 16, the maximum pressure for all the presented points are below the peak pressure limit. By excluding points with NOx emissions higher than the Tier III limit (2.01 g/kW/h) or with maximum average pressure higher than the peak pressure limit

(200 bar) as well as with knock occurrence, there are 11, 17 and 12 points that can be identified for a

potential engine optimisation at 1800 r/min, 1629 r/min and 1457 r/min operation conditions, respectively.

The variations of the derived NOx emissions and BSFC at the investigated engine speeds are presented

in Table 10, Table 11 and Table 12. As mentioned above, the NG mass variation causes an inevitable

change to the operation load, thus the brake power variation is also included in Table 10, Table 11 and

Table 12.

Table 10 provides the 11 potential optimal solutions at 1800 r/min, which can be selected by the following

criteria: (1) maximum simultaneous reduction of the BSFC and NOx emission; (2) maximum BSFC

reduction and NOx emission equals or less than the Tier III limit; (3) maximum NOx emission reduction

and BSFC equals or less than the reference value. As indicated by Table 10, there is no point meeting the

first criterion, i.e., simultaneously achieving maximum reductions of BSFC and NOx emissions.

However, points 7, 8, 9, 10 and 11 could provide a compromise by simultaneously reducing BSFC and

NOx emissions with different scales. For the second criterion, point 3 is the optimised case with –7.5°CA

pilot injection timing, +5% equivalence ratio variation and +20% NG mass variation, resulting in the

maximum reduction of 8.20% in BSFC and 5.98% increase in NOx emission. Nevertheless, the absolute

NOx emissions of point 3 (1.77 g/kW/h) is still below the Tier III limit (2.01 g/kW/h). The operating

settings of point 11, which are –5 °CA pilot injection timing, 0% equivalence ratio variation and 20%

NG mass variation, leads to the maximum reduction (10.78%) in NOx emissions and minor reduction

(1.48%) in BSFC. Thus, point 11 is the optimal solution for the third criterion. It must be noted that the

brake power of all the optimal points at 1800 r/min increase at a scale ranging from 0.56% to 29.0%.

Point 7 provides the closest brake power (0.56% variation) to the baseline case and a simultaneous

reduction of NOx emissions and BSFC.

Table 10 Optimal points obtained from the parametric investigation at 1800 r/min

No.	ID	SOI	$\Delta\lambda$	Δm_{NG}	ΔP_b	ΔNOx	ΔBSFC
-	-	°CA	%	%	%	%	%
0	Baseline	−5	0	0	-	-	-
1	A1B3C1	−7.5	+5	0	6.50	13.77	−6.13
2	A1B3C2	−7.5	+5	10	17.90	11.38	−7.38
3	A1B3C3	−7.5	+5	20	29.00	5.98	−8.20
4	A2B2C1	−6.25	0	0	5.80	20.11	−5.52
5	A2B2C2	−6.25	0	10	16.60	17.96	−6.36
6	A2B2C3	−6.25	0	20	27.26	12.57	−6.96
7	A2B3C1	−6.25	+5	0	0.56	−2.99	−0.56
8	A2B3C2	−6.25	+5	10	11.67	−8.38	−2.23
9	A2B3C3	−6.25	+5	20	22.38	−9.58	−3.25
10	A3B2C2	−5	0	10	9.69	−6.59	−0.46
11	A3B2C3	−5	0	20	20.18	−10.78	−1.48

Table 11 Optimal points obtained from the parametric run at 1629 r/min

No.	ID	SOI	$\Delta\lambda$	Δm_{NG}	ΔP_b	ΔNOx	ΔBSFC
-	-	°CA	%	%	%	%	%
0	Baseline	−5	0	0	-	-	-
1	A1B2C1	−7.5	0	0	15.06	32.69	−13.09
2	A1B2C2	−7.5	0	10	25.84	32.52	−13.29
3	A1B2C3	−7.5	0	20	37.41	29.35	−13.96
4	A1B3C1	−7.5	5	0	5.98	25.23	−5.64
5	A1B3C2	−7.5	5	10	15.35	23.43	−5.41
6	A1B3C3	−7.5	5	20	25.89	21.13	−6.09
7	A2B1C1	−6.25	−5	0	15.35	28.26	−13.31
8	A2B1C2	−6.25	−5	10	26.08	26.60	−13.46
9	A2B1C3	−6.25	−5	20	37.82	26.62	−14.21
10	A2B2C1	−6.25	0	0	7.48	15.74	−6.96
11	A2B2C2	−6.25	0	10	18.38	14.44	−7.83
12	A2B2C3	−6.25	0	20	26.55	10.87	−6.58
13	A3B1C1	−5	−5	0	8.52	9.59	−7.85
14	A3B1C2	−5	−5	10	18.86	9.13	−8.20
15	A3B1C3	−5	−5	20	29.61	7.98	−8.78
16	A3B2C2	−5	0	10	9.82	−0.97	−0.64
17	A3B2C3	−5	0	20	19.25	−2.57	−0.86

The NOx and BSFC reductions of the 17 potential optimal solutions at 1629 r/min are presented in Table 11. As inferred from Table 11, only points 16 and 17 achieve simultaneous reduction of BSFC and NOx emissions whilst the BSFC reduction scales of these two points are very small (−0.6% and −0.9%, respectively) compared to those of other potential optimal points. The NOx emissions of the rest 15 points are higher than the reference case but still below the Tier III limit. The maximum BSFC reduction (−14.2%) is achieved at point 9, which is with +6.25°CA pilot injection timing, −5% equivalence ratio variation and +20% NG mass variation. The operating settings of point 17, which is −5°CA pilot injection timing, 0% equivalence ratio variation and 20% NG mass variation, results in the maximum NOx

reduction (–2.57%). The maximum increase of brake power (37.82%) is observed at point 9, which also provides the maximum BSFC reduction.

Table 12 Optimal points obtained from the parametric run at 1457 r/min

No.	ID	SOI	$\Delta\lambda$	Δm_{NG}	ΔP_b	ΔNOx	ΔBSFC
-	-	°CA	%	%	%	%	%
0	Baseline	–5	0	0	-	-	-
1	A1B2C3	–7.5	0	10	21.57	21.11	–10.42
2	A1B3C2	–7.5	5	0	3.15	20.27	–3.06
3	A1B3C3	–7.5	5	10	11.11	16.39	–1.98
4	A2B1C2	–6.25	–5	0	18.96	23.04	–15.94
5	A2B1C3	–6.25	–5	10	26.42	15.30	–13.86
6	A2B2C1	–6.25	0	–10	1.42	21.76	–10.18
7	A2B2C2	–6.25	0	0	6.65	11.95	–6.24
8	A2B2C3	–6.25	0	10	13.55	7.49	–4.09
9	A3B1C1	–5	–5	–10	6.90	22.41	–14.78
10	A3B1C2	–5	–5	0	12.84	10.62	–11.38
11	A3B1C3	–5	–5	10	19.63	2.33	–8.97
12	A3B2C1	–5	0	–10	–4.85	8.74	–4.26

Table 12 provides the derived NOx and BSFC reductions of the 12 potential optimal solutions at 1457 r/min. As inferred from **Error! Reference source not found.**, the NOx emissions of all the potential optimal solutions are higher than that of reference case, thus there is no solution for the first and third selection criterion. For the second criterion, point 4 is the optimised case with –6.25°CA pilot injection timing, –5% equivalence ratio variation and 0% NG mass variation, resulting in the maximum BSFC reduction of 15.9% while the corresponding NOx emissions comply with the Tier III limit. In addition, optimal points exhibit an increased brake power except point 12, which provides a simultaneous reduction of brake power and BSFC.

5. Conclusions

This study reported the development and validation of a 3D CFD model developed in the CONVERGE software, which was employed to investigate the operating settings effects on combustion, knocking occurrence, performance and emissions of marine dual fuel engines, as well as to perform a parametric study for identifying the optimal operating settings for NOx emissions and BSFC reduction at three operating conditions (1800 r/min, 1629 r/min and 1457 r/min). The main findings of this study are

summarised as follow.

1. The developed 3D CFD model is capable of predicting the heat release rate, engine performance and emissions (NOx, CO and HC) of marine dual fuel engines with adequate accuracy.

2. As inferred from the effects investigation at 100% load, retarding the pilot injection timing or increasing equivalence ratio leads to increased BSFC and reduced NOx emissions, whereas increasing the natural gas injection mass could result in simultaneous reduction of BSFC and NOx emissions.

3. As inferred from effects investigation at 100% load, the knock index and the maximum peak pressure decrease simultaneously with retarding the pilot injection timing, reducing the equivalence ratio or reducing the natural gas mass. The advance of the pilot injection timing turns out to be a key factor for stimulating the knocking occurrence.

4. As inferred from the parametric runs, the optimal solution at 1800 r/min and 1629 r/min operation conditions can be achieved by controlling the pilot injection timing, equivalence ratio variation and NG mass variation within –5 to –7.5 °CA, –5% to +5% and 0% to +20%, respectively. For the 1457 r/min operation condition, the appropriate ranges of pilot injection timing and the equivalence ratio variation are the same with those at 1800 r/min and 1629 r/min, whilst the NG mass variation range should be between –10% and +10%.

5. By analysing the performance-emissions trade-off at three engine operating points, settings that lead to potential BSFC reduction are identified, whilst the NOx emissions comply with the Tier III NOx emissions regulation.

This study contributes to the thorough and comprehensive understanding of the combustion characteristics, emissions formation and knocking occurrence in diesel-natural gas DF engines. The

derived CFD results are expected to support the combustion analysis and enhancement of marine DF engines during the design phase, whilst the derived optimal solution is expected to provide guidelines of DF engine management for reducing operating cost and environmental footprint.

However, there are several limitation in this study. The parametric investigation is performed considering only the NOx emissions and BSFC, whilst the HC emissions are not considered due to the model's incapacity to characterize the methane slip. Future studies can focus on the gas-exchange process for additionally predicting the HC emissions by incorporating the inlet and exhaust ports with the cylinder model. Besides, intelligent multi-objective optimisation algorithms can be used jointly with the 3D CFD model to obtain the optimal settings targeting improved combustion behaviour for achieving high engine performance and low emissions.

Acknowledgements

References

1. Shrivastava, K., S. Thipse, and I. Patil, *Optimization of diesel engine performance and emission parameters of Karanja biodiesel-ethanol-diesel blends at optimized operating conditions.* Fuel, 2021. **293**: p. 120451.
2. Jain, A., A.P. Singh, and A.K. Agarwal, *Effect of split fuel injection and EGR on NOx and PM emission reduction in a low temperature combustion (LTC) mode diesel engine.* Energy, 2017. **122**: p. 249-264.
3. Tan, D., et al., *Performance optimization of a diesel engine fueled with hydrogen/biodiesel with water addition based on the response surface methodology.* Energy, 2023. **263**: p. 125869.
4. Kumar, N.R., C. Sekhar, and S. Adinarayana, *Effects of compression ratio and EGR on performance, combustion and emissions of DI injection diesel engine.* International Journal of Applied Science and Engineering, 2013. **11**(1): p. 41-49.
5. Maiboom, A. and X. Tauzia, *NOx and PM emissions reduction on an automotive HSDI Diesel engine with water-in-diesel emulsion and EGR: An experimental study.* Fuel, 2011. **90**(11): p. 3179-3192.
6. Kang, W., et al., *PM and NOx reduction characteristics of LNT/DPF+ SCR/DPF hybrid system.* Energy, 2018. **143**: p. 439-447.
7. Vasilescu, M.-V., et al. *Research on Exhaust Gas Cleaning System (EGCS) used in shipping industry for reducing SOx emissions.* in *E3S Web of Conferences.*

2021. EDP Sciences.

8. Baldissone, G., M. Demichela, and D. Fissore, *Lean VOC-air mixtures catalytic treatment: Cost-benefit analysis of competing technologies.* Environments, 2017. **4**(3): p. 46.

9. Lepitzki, J. and J. Axsen, *The role of a low carbon fuel standard in achieving long-term GHG reduction targets.* Energy Policy, 2018. **119**: p. 423-440.

10. Deng, J., et al., *A review of NOx and SOx emission reduction technologies for marine diesel engines and the potential evaluation of liquefied natural gas fuelled vessels.* Science of The Total Environment, 2020: p. 144319.

11. Thomson, H., J.J. Corbett, and J.J. Winebrake, *Natural gas as a marine fuel.* Energy Policy, 2015. **87**: p. 153-167.

12. Thomson, H., J.J. Corbett, and J.J. Winebrake, *Natural gas as a marine fuel.* Energy Policy, 2015. **87**(December): p. 153-167.

13. Stoumpos, S., et al., *Marine dual fuel engine modelling and parametric investigation of engine settings effect on performance-emissions trade-offs.* Ocean Engineering, 2018. **157**: p. 376-386.

14. Wang, H., H. Gan, and G. Theotokatos, *Parametric investigation of pre-injection on the combustion, knocking and emissions behaviour of a large marine four-stroke dual-fuel engine.* Fuel, 2020. **281**: p. 118744.

15. Bhandari, K., et al., *Performance and emissions of natural gas fueled internal combustion engine: A review.* 2005.

16. Crookes, R.J., T. Korakianitis, and A.M. Namasivayam. *A systematic experimental assessment of the use of rapeseed methyl ester (RME) as a compression ignition engine fuel during conventional and dual-fuel operation.* in *TAE 7th International Colloquium on Fuels. Stuttgart.* 2009.

17. Park, S. and S. Song, *Model-based multi-objective Pareto optimization of the BSFC and NOx emission of a dual-fuel engine using a variable valve strategy.* Journal of Natural Gas Science and Engineering, 2017. **39**: p. 161-172.

18. Mustafi, N.N., R.R. Raine, and S. Verhelst, *Combustion and emissions characteristics of a dual fuel engine operated on alternative gaseous fuels.* Fuel, 2013. **109**: p. 669-678.

19. Lounici, M.S., et al., *Towards improvement of natural gas-diesel dual fuel mode: An experimental investigation on performance and exhaust emissions.* Energy, 2014. **64**: p. 200-211.

20. Heywood, J.B., *Internal combustion engine fundamentals.* Vol. 9. 1988: Mcgraw-hill New York. 457.

21. Yao, C., A. Yao, and H. Xu, *Mechanism of internal combustion engine detonation and its damage to combustion chamber components.* 2015: Science Press.

22. Wang, Z., H. Liu, and R.D. Reitz, *Knocking combustion in spark-ignition engines.* 2017. **61**: p. 78-112.

23. Baldi, F., G. Theotokatos, and K. Andersson, *Development of a combined mean value–zero dimensional model and application for a large marine four-stroke Diesel engine simulation.* Applied Energy, 2015. **154**: p. 402-415.

24. Priesching, P., et al., *About Describing the Knocking Combustion in Gasoline and Gas Engines by CFD Methods.* 2015, SAE Technical Paper.

25. Maghbouli, A., et al., *A multi-dimensional CFD-chemical kinetics approach in detection and reduction of knocking combustion in diesel-natural gas dual-fuel engines using local heat release analysis.* SAE International Journal of Engines, 2013. **6**(2013-01-0865): p. 777-787.

26. Abagnale, C., et al., *Combined numerical-experimental study of dual fuel diesel engine.* Energy procedia, 2014. **45**: p. 721-730.

27. Maghbouli, A., et al., *Numerical study of combustion and emission characteristics of dual-fuel engines using 3D-CFD models coupled with chemical kinetics.* Fuel, 2013. **106**: p. 98-105.

28. Chintala, V. and K. Subramanian, *A CFD (computational fluid dynamics) study for optimization of gas injector orientation for performance improvement of a dual-fuel diesel engine.* Energy, 2013. **57**: p. 709-721.

29. Mattarelli, E., C.A. Rinaldini, and V.I. Golovitchev, *CFD-3D analysis of a light duty Dual Fuel (Diesel/Natural Gas) combustion engine.* Energy Procedia, 2014. **45**: p. 929-937.

30. Maurya, R.K. and P. Mishra, *Parametric investigation on combustion and emissions characteristics of a dual fuel (natural gas port injection and diesel pilot injection) engine using 0-D SRM and 3D CFD approach.* Fuel, 2017. **210**: p. 900-913.

31. Li, Y., et al., *A numerical investigation on methane combustion and emissions from a natural gas-diesel dual fuel engine using CFD model.* Applied Energy, 2017. **205**: p. 153-162.

32. Shu, J., et al., *Experimental and computational study on the effects of injection timing on thermodynamics, combustion and emission characteristics of a natural gas (NG)-diesel dual fuel engine at low speed and low load.* Energy conversion and management, 2018. **160**: p. 426-438.

33. Morii, Y., et al., *Two-dimensional laboratory-scale DNS for knocking experiment using n-heptane at engine-like condition.* Combustion and Flame, 2021. **223**: p. 330-336.

34. Wei, H., et al., *Experimental investigation on knocking combustion characteristics of gasoline compression ignition engine.* Energy, 2018. **143**: p. 624-633.

35. Corti, E. and C. Forte, *Statistical analysis of indicating parameters for knock detection purposes.* 2009, SAE Technical Paper.

36. Worret, R., et al., *Application of different cylinder pressure based knock detection methods in spark ignition engines.* 2002, SAE Technical Paper.

37. Zhen, X., et al., *The engine knock analysis–an overview.* Applied Energy, 2012. **92**: p. 628-636.

38. Feng, H., et al., *Analysis of auto-ignition characteristics of low-alcohol/iso-octane blends using combined chemical kinetics mechanisms.* Fuel, 2018. **234**: p. 836-849.

39. Zhen, X. and Y. Wang, *Numerical analysis of knock during HCCI in a high compression ratio methanol engine based on LES with detailed chemical kinetics.* Energy Conversion and Management, 2015. **96**: p. 188-196.

40. Sazhin, S., et al., *The Shell autoignition model: a new mathematical formulation.* Combustion and flame, 1999. **117**(3): p. 529-540.

41. Wang, Z., F. Li, and Y. Wang, *A generalized kinetic model with variable octane number for engine knock prediction.* Fuel, 2017. **188**: p. 489-499.

42. Pan, J., G. Shu, and H. Wei, *Research on in-cylinder pressure oscillation characteristic during knocking combustion in spark-ignition engine.* Fuel, 2014. **120**: p. 150-157.

43. Livengood, J. and W. PC, *Correlation of autoignition phenomena in internal combustion engines and rapid compression machines.* 1955.

44. CONVERGE, *CONVERGE 2.4 Manual.* 2018: Convergent Science, Inc.

45. Reitz, R.D. and R. Diwakar, *Structure of high-pressure fuel sprays.* SAE transactions, 1987: p. 492-509.

46. Beale, J.C. and R.D. Reitz, *Modeling spray atomization with the Kelvin-Helmholtz/Rayleigh-Taylor hybrid model.* Atomization and sprays, 1999. **9**(6).

47. Amsden, A., *A computer program for chemically reactive flows with sprays.* Report of Los Alamos National Laboratory, 1989.

48. Senecal, P., et al., *Multi-dimensional modeling of direct-injection diesel spray liquid length and flame lift-off length using CFD and parallel detailed chemistry.* SAE transactions, 2003: p. 1331-1351.

49. Rahimi, A., E. Fatehifar, and R.K. Saray, *Development of an optimized chemical kinetic mechanism for homogeneous charge compression ignition combustion of a fuel blend of n-heptane and natural gas using a genetic algorithm.* Proceedings of the Institution of Mechanical Engineers, Part D: Journal of Automobile Engineering, 2010. **224**(9): p. 1141-1159.

50. Han, Z. and R.D. Reitz, *Turbulence modeling of internal combustion engines using RNG κ-ε models.* Combustion science and technology, 1995. **106**(4-6): p.

267-295.

51. O'Rourke, P.J. and A. Amsden, *A spray/wall interaction submodel for the KIVA-3 wall film model.* SAE transactions, 2000: p. 281-298.

52. Reitz, R.D., *Mechanism of breakup of round liquid jets.* Encyclopedia of fluid mechanics, 1986. **10**.

53. Senecal, P., et al., *A new parallel cut-cell Cartesian CFD code for rapid grid generation applied to in-cylinder diesel engine simulations*. 2007, SAE Technical Paper.

54. Horvath, A., *Redlich-Kwong equation of state: review for chemical engineering calculations.* Chemical Engineering Science, 1974. **29**(5): p. 1334-1340.

55. Senecal, P.K., *Development of a methodology for internal combustion engine design using multi-dimensional modeling with validation through experiments.* 2001.

56. Turns, S.R., *Introduction to combustion*. Vol. 287. 1996: McGraw-Hill Companies.

57. Xiang, L., et al., *Parametric knocking performance investigation of spark ignition natural gas engines and dual fuel engines.* Journal of Marine Science and Engineering, 2020. **8**(6): p. 459.

58. AVL, *Pressure sensor for combustion analysis - GU22CK*. 2016.

59. KISTLER, *Measurement and evaluation system for combustion analysis on test benches and in vegicles - KiBox To Go 2893B*. 2019: Switzerland.

60. AVL. *AVL Fuel Mass Flow Meter and Fuel Temperature Control*. 2019; Available from: https://www.avl.com/-/avl-fuel-mass-flow-meter-and-fuel-temperature-control.

61. Endress+Hauser. *Proline Promass 83F Coriolis flowmeter*. 2019; Available from: https://www.uk.endress.com/en/field-instruments-overview/flow-measurement-product-overview/Product-Coriolis-flowmeter-Proline-Promass-83F.

62. ABB. *Thermal mass flowmeter: Sensyflow FMT700-P and FMT700-P Compact*. 2019; Available from: https://new.abb.com/products/measurement-products/flow/thermal-mass-flowmeters/sensyflow-fmt700-p.

63. AVL, *Pressure sensor for combustion analysis - LP11DA*. 2016.

64. AVL. *AMA i60 exhaust measurement system*. 2013; Available from: https://www.avl.com/-/avl-fuel-mass-flow-meter-and-fuel-temperature-control.

65. Bonalivi, *GS5969 E Natural gas chromatographic analyzer.* 2020

66. PetroChina. 2020; Available from: http://www.petrochina.com.cn/ptr/.

67. Taskar, B., et al., *The effect of waves on engine-propeller dynamics and propulsion performance of ships.* Ocean Engineering, 2016. **122**: p. 262-277.

68. Zhou, D., et al., *Application of CFD-chemical kinetics approach in detecting RCCI engine knocking fuelled with biodiesel/methanol.* Applied Energy, 2015. **145**: p. 255-264.

69. Li, A., Z. Zheng, and T. Peng, *Effect of water injection on the knock, combustion, and emissions of a direct injection gasoline engine.* Fuel, 2020. **268**: p. 117376.

70. Liang, L., et al., *Modeling knock in spark-ignition engines using a G-equation combustion model incorporating detailed chemical kinetics*. 2007, SAE Technical Paper.

71. Ding, Y., et al., *A new method to smooth the in-cylinder pressure signal for combustion analysis in diesel engines.* Proceedings of the Institution of MechanicalEngineers-A, 2011. **225**(3): p. 309.

72. Chen, H., P.M. Lillo, and V. Sick, *Three-dimensional spray–flow interaction in a spark-ignition direct-injection engine.* International Journal of Engine Research, 2016. **17**(1): p. 129-138.

73. Hao, C., et al. *Influence of Early and Late Fuel Injection on Air Flow Structure and Kinetic Energy in an Optical SIDI Engine*. in *WCX World Congress Experience*. 2018.

74. Ryu, K., *Effects of pilot injection timing on the combustion and emissions characteristics in a diesel engine using biodiesel–CNG dual fuel.* Applied Energy, 2013. **111**: p. 721-730.

75. Zheng, J., et al., *Effect of equivalence ratio on combustion and emissions of a dual-fuel natural gas engine ignited with diesel.* Applied Thermal Engineering, 2019. **146**: p. 738-751.

76. Yang, B., et al., *Comparison study the particulate matter characteristics in a diesel/natural gas dual-fuel engine under different natural gas-air mixing operation conditions.* Fuel, 2021. **288**: p. 119721.

77. Papagiannakis, R. and D. Hountalas, *Experimental investigation concerning the effect of natural gas percentage on performance and emissions of a DI dual fuel diesel engine.* Applied Thermal Engineering, 2003. **23**(3): p. 353-365.

78. Zhu, L., et al., *Effects of fuel reforming on large-bore low-speed two-stroke dual fuel marine engine combined with EGR and injection strategy.* International Journal of Hydrogen Energy, 2020. **45**(53): p. 29505-29517.

79. Yang, B., et al., *Effects of pilot injection timing on the combustion noise and particle emissions of a diesel/natural gas dual-fuel engine at low load.* Applied Thermal Engineering, 2016. **102**: p. 822-828.

80. Ickes, A., et al., *Impact of cetane number on combustion of a gasoline-diesel dual-fuel heavy-duty multi-cylinder engine.* SAE International Journal of Engines, 2014. **7**(2): p. 860-872.